Title
Inhibiting Microbial Growth, Virulence, and Motility via Bioinspired Nanotopography

Author
Rosenzweig, Rachel

Publication Date
2020

Peer reviewed|Thesis/dissertation

UNIVERSITY OF CALIFORNIA,
IRVINE

Inhibiting Microbial Growth, Virulence, and Motility *via* Bioinspired Nanotopography

DISSERTATION

submitted in partial satisfaction of the requirements
for the degree of

DOCTOR OF PHILOSOPHY

in Materials Science and Engineering

by

Rachel Rosenzweig

Dissertation Committee:
Professor Albert F. Yee, Chair
Professor Michelle A. Digman
Professor Albert Siryaporn

2020

TABLE OF CONTENTS

LIST OF FIGURES

LIST OF TABLES

ACKNOWLEDGMENTS

***

Prof. Yee, Prof. Digman, Prof. Siryaporn, Prof. Pearlman, Dr. Behzad Rad
Co-Authors | Committee Members | Collaborators | Mentors
for providing your labs & remarkable expertise!

Dr. Kumar Perinbam, Dr. Siavash Ahrar, Michaela Marshall
Co-Authors | Research Extraordinaires
for teaching me your ways!

Dr. Mary Nora Dickson, Dr. Elena I. Liang
Predecessors | Cherished Friends
for supporting & inspiring me!

Xin Fu, Yassi Fatapour, Jingyi Luo
Labmates | Boba Buddies
for keeping me sane!

Van K. Ly, Alex Parivar
Co-Authors | Mentees
for encouraging me!

My Family!

***

I acknowledge the American Chemical Society for permission to include copyrighted materials as part of my dissertation originally published in ACS Applied Materials and Interfaces and ACS Applied Bio Materials. Financial support was provided by the UCI Department Materials Science and Engineering, UCI UROP and MDP Programs, UCI Applied Innovation, Department of Defense Peer Reviewed Medical Research Program Award No. W81XWH-17-0355, UCI Irvine Materials Research Institute, Lawrence Berkeley National Laboratory Molecular Foundry, UCI AGS, and UCI Public Impact Distinguished Fellowship.

VITA

Rachel Rosenzweig

2020 **University of California, Irvine |** Ph.D. Materials Science & Engineering
2018 **University of California, Irvine |** M.S. Materials Science & Engineering
2015 **University of Washington, Seattle |** B.S. Materials Science & Engineering

FELLOWSHIPS & AWARDS

2019 **UCI Grad Slam Champion |** UCI Graduate Division Public Speaking Competition
2018 **Public Impact Distinguished Fellowship |** UCI Graduate Division
2018 **AGS Conference Travel Grant |** UCI Associated Graduate Students
2017 **New Venture Competition- Honorable Mention |** UCI Applied Innovation
2016 **Multidisciplinary Design Program Fellowship |** UCI UROP & Calit2
2015 **Diversity Recruitment Fellowship |** UCI Dept. Materials Science & Engineering

PUBLICATIONS

Rosenzweig, R.; Marshall, M.; Parivar, A.; Ly, V. K.; Pearlman, E.; Yee, A. F. Biomimetic Nanopillared Surfaces Inhibit Drug Resistant Filamentous Fungal Growth. *ACS Appl. Bio Mater.* **2019**, *2*, 3159-3163.

Rosenzweig, R.; Perinbam, K.; Ly, V. K.; Ahrar, S.; Siryaporn, A.; Yee., A. F. Nanopillared Surfaces Disrupt *Pseudomonas aeruginosa* Mechanoresponsive Upstream Motility. *ACS Appl. Mater. Interfaces* **2019**, *11*, 10532-10539.

Hassanzadeh, P.; Kazemzadeh-Narbat, M.; **Rosenzweig, R.**; Zhang, X.; Khademhosseini, A.; Annabi, N.; Rolandi, M. Ultrastrong & Flexible Hybrid Hydrogels Based on Solution Self-Assembly of Chitin Nanofibers in Gelatin Methacryloyl. *J. Mater. Chem. B* **2016**,*4*,2539-2543.

CONFERENCE PRESENTATIONS

Molecular Foundry User Meeting, Berkeley, CA, 2019.
Gordon Research Conference Microbial Adhesion & Signal Transduction, Newport, RI, 2019.
Pacific Rim Symposium on Surfaces, Coatings, & Interfaces, Waikoloa Beach, HI, 2018.
Military Health System Research Symposium, Kissimmee, FL, 2018.
Materials Research Society Spring Meeting & Exhibit, Phoenix, AZ, 2018.
American Physical Society March Meeting, Los Angeles, CA, 2018.
Biophysical Society Annual Meeting, San Francisco, CA, 2018.

ABSTRACT OF THE DISSERTATION

Inhibiting Microbial Growth, Virulence, and Motility *via* Bioinspired Nanotopography

By

Rachel Rosenzweig

Doctor of Philosophy in Materials Science and Engineering

University of California, Irvine, 2020

Professor Albert F. Yee, Chair

Pathogenic microbes, such as bacteria and fungi, often contaminate medical systems resulting in 1.7 million annual cases of hospital acquired infections, 99,000 annual deaths, and $16.6 billion spent in healthcare costs in US alone. Current solutions declining in efficacy are drug therapies, which have led to the rise of antimicrobial resistance and created an urgent need for alternative strategies. Here, the fabrication and physical antimicrobial effects of polymeric nanoimprinted surfaces based on bactericidal nanotopography inspired by nature are explored. A materials science and engineering approach is combined with microbiology and mechanobiology to further probe the cell-surface interface for the the ability of the bioinspired nanotopography to (1) hinder surface-attached *Pseudomonas aeruginosa* bacterial growth and virulence, (2) disrupt *P. aeruginosa* bacterial mechanoresponsive upstream motility in fluid flow, and (3) inhibit *Aspergillus fumigatus* and *Fusarium oxysporum* filamentous fungal growth demonstrating antimicrobial effects in a eukaryotic cell type system. This work promises broad applications for synergistic antimicrobial solutions in medically relevant systems and heralds new platforms to study mechanobiology.

CHAPTER 1. Introduction- Antibacterial Bioinspired Nanotopography and Fabrication

Introduction

Bacteria and fungi can populate and form biofilms, or surface-attached cellular communities protected by secreted extracellular polymeric substance (EPS). Biofilms harboring infectious pathogens often form in medically relevant environments.[1] There are 1.7 million cases of hospital acquired infections each year due to contaminated medical devices resulting in 99,000 deaths[2] and $16.6 billion dollars spent in healthcare costs in the US alone.[3] Frequently contaminated medical devices and implants include hearing implants, contact lenses,[4] cardiac implants,[5,6] joint implants,[7] and catheters.[8,9]

Current solutions declining in efficacy include the use of antimicrobials, which has led to the rise of antimicrobial resistance (AMR). AMR has been declared by the World Health Organization as a dominant threat to global health, the economy, and environment with annual death rates predicted to surpass those from cancer by 2050.[10] A major cause of AMR is the formation of bacterial and fungal biofilms that harbor pathogens, which result in a 10 to 1000-fold drug diffusion decrease and are responsible for 80% of clinical infections.[11,12]

When these microbes attach to surfaces, they secrete autoinducer signaling molecules to communicate to other microbes using the process known as quorum sensing.[13] Once these microbes begin to form a microcolony, they synthesize a protective EPS that significantly decreases diffusion of antimicrobial drugs. Eventually, these biofilms

begin to mature and form antimicrobial degrading enzymes and disperse more AMR microbes to contaminate other surfaces.[14] Bacteria and fungi also possess the ability to alter their gene expression within biofilms and at the single cellular level leading to AMR. Mechanisms of AMR include the formation of efflux pumps to rid the cells of antimicrobial drugs, the development of antimicrobial degrading enzymes, and the mutations of antimicrobial binding proteins.[15] There is an unmet need to prevent pathogenic microbial growth, virulence, and motility on surfaces without the use of antimicrobial chemicals that can lead to resistance.

One of the approaches to discovering antimicrobial surfaces is to look to nature for inspiration. Antifouling surface effects have been found in nature from the micron-scale to the nano-scale. These include Galapagos shark skin,[16] lotus leaves,[17] dragonfly wings,[18] gecko feet,[19] and Megapodiidae eggshells,[20] to name a few. Such surfaces consist of pillared arrays sometimes smaller than the wavelength of visible light have been mimicked and engineered by various research groups for applications in biosensing[21,22] and antibacterial surfaces.[23] In this work, we utilize a low-cost technique known as nanoimprint lithography (NIL) to fabricate bioinspired nanotopographic surfaces inspired by antifouling cicada wings on poly(methyl methacrylate) (PMMA),[24,25] an FDA approved polymer commonly used for medical devices. The NIL technique can be easily extended to other thermoplastic polymer materials if desired. We use NIL for our applications due to the reusability of imprinting molds, feasibility for medical devices relevant polymers, and scalability.

Results and Discussion

We begin by ordering commercial imprinting molds (Temicon, GmbH) or fabricating a nanoimprint lithography mold on a four-inch silicon (100) wafer. A base-plating mask of 10nm chromium was applied to facilitate a conductive layer easily bonded to the Si/SiO2. Next, a ZEP 50% positive photoresist (1:1: copolymer of alpha-chloromethacrylate and alpha-methylstyrene) was spincoated and developed using an n-amyl acetate on the wafer at 3000rpm and then baked at 100°C. Then, electron beam lithography (EBL) was conducted to pattern nanoscale holes into the photoresist using a Vistec VB300 Electron Beam Lithography System. Next, highly anisotropic fluorine inductively coupled plasma (ICP) with SF_6/O_2 at 40sccm flow rate was used to etch 300nm of the exposed silicon nanopatterns using an Oxford PlasmaLab 150 Inductively Coupled Etcher fluorine. Subsequently, the ZEP 50% photoresist layer was removed using a dimethylacetamide organic solvent (**Figure 1A**). Finally, the 300nm tall and 100nm wide nanopillar structures were exposed with center-to-center periodicities ranging from 200nm to 500nm in a square array (**Figure 1B**).

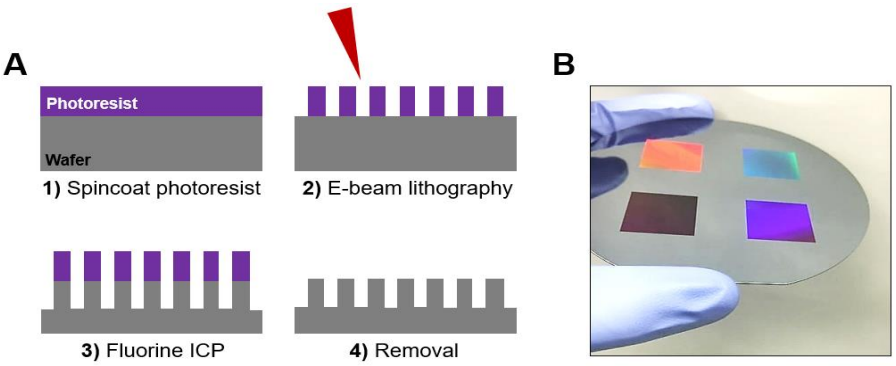

Figure 1. Fabrication of silicon molds with nanotopography. **(A)** First, a ZEP 50% positive photoresist was spincoated at 3000rpm onto a 10nm chromium masked silicon (100) wafer. Then, electron beam lithography was used to pattern nanoscale holes in the ZEP 50%. Next, fluorine ICP was using to etch the silicon exposed by the photoresist using a SF6/O2 flow rate of 40sccm. Subsequently, the photoresist was removed using a dimethylacetamide organic solvent. Finally, the nano pillared structures were exposed revealing **(B)** 300nm tall and 100nm wide pillars with a 200nm, 300nm, 400nm, or 500nm pitch in square arrays.

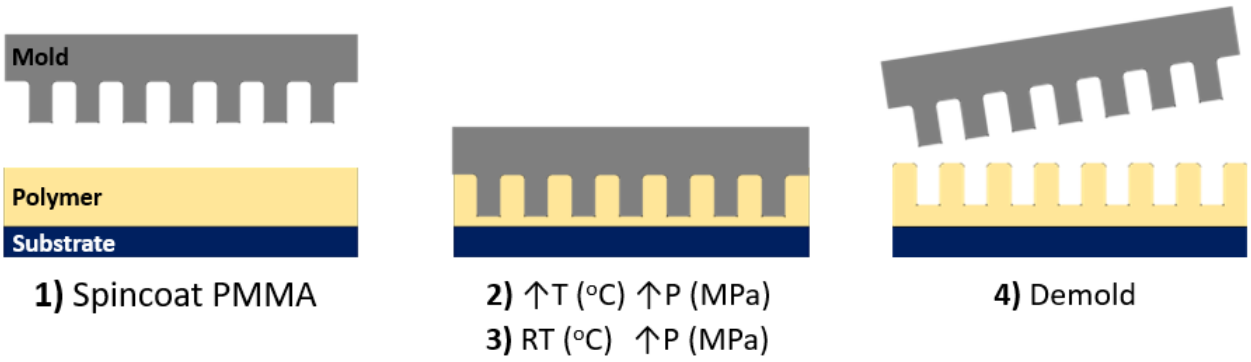

Figure 2. Schematic of nanoimprint lithography (NIL) process. First, a 5% PMMA solution is spincoated and annealed on a glass substrate. Then, the sample is transferred to a hot embosser heated to 70°C above the PMMA glass transition temperature (T_g) with a pressure of 2MPa applied for 20 minutes. Finally, the hot embosser is cooled to room temperature with the applied pressure held for 10 minutes before demolding to expose the PMMA nanopillared surface structures.

The molds commercially ordered or custom fabricated are maintained and stored for nanoimprint lithography processes. The NIL process previously described[26,27] involves first spincoating a 5% PMMA solution in toluene on a glass substrate at 6000rpm for 45seconds before annealing. Then, the sample is transferred to a hot embosser to raise the temperature to 70°C above the PMMA glass transition temperature (T_g=105°C) with an applied pressure of 2MPa for 20 minutes. Finally, the temperature is lowered to room temperature with the applied pressure held for 10 minutes before demolding to expose the PMMA nanopatterns (**Figure 2**). Sample preparation was followed by scanning electron microscopy characterization previously described[26] to image the nanopillared surface patterns (**Figure 3**). The lettering in the nomenclature represents the nanoimprinting mold originated from a cicada wing or pillared master mold (Temicon GmbH), while the numeric in the nomenclature represented the center-to-center pillar periodicities nanometers (**Table 1**). The tip packing fraction represents the total surface area at the pillar tips, while

the contact angles represent degrees of hydrophobicity. Molds used for these surfaces were commercially ordered and created through light interference lithography (Temicon GmbH).

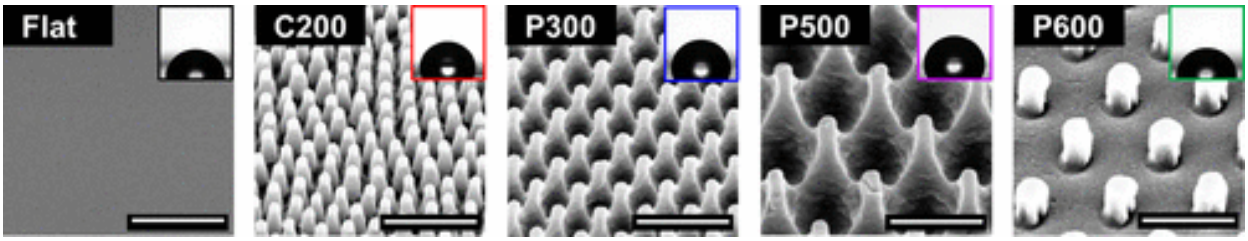

Figure 3. Scanning electron micrographs (SEMs) of PMMA surfaces taken at a 45° tilt with 3 kV, using the FEI Magellan SEM. Flat surfaces were prepared through spin coating. Nanostructured surfaces were fabricated through nanoimprint lithography (NIL) to form C200, P300, P500, and P600 surfaces. The lettering represented the negative imprinting mold originating from a cicada wing or pillared master mold. The numeric in the nomenclature represented nanometer values in center-to-center pillar periodicities per surface. Scale bars represent 500 nm. Contact angles for each surface are included as their insets to measure degrees of hydrophobicity and were taken using a OneAttention Theta Optical Tensiometer.

Table 1. Dimensional Feature Measurements of the Nanopillared Surfaces[a]

surface	period (nm)	width (nm)	height (nm)	tip packing fraction Φ	contact angle θ
C200	170	70	210	0.18	110 ± 0.8
P300	320	120	300	0.28	117 ± 0.5
P500	500	100	700	0.04	122 ± 0.6
P600	595	215	300	0.22	93 ± 0.4

[a] Period, width, and height indicate feature measurements of individual nanopillars per surface. Tip packing fraction, Φ, indicates the ratio of the pillar tip surface area to the substrate surface area. θ indicates contact angle values. n = 5 for each surface. Standard errors are given for each average contact angle per surface.

Conclusions and Applications

In summary, we fabricated nanopillared surface molds in various pillar geometries for NIL using EBL and fluorine ICP. We also described the process of NIL using commercially ordered molds (Temicon, GmbH) to fabricate nanopillared surfaces of PMMA to study antimicrobial cell-surface interface effects. We aim to apply these surfaces to study

the cell-surface interaction of pathogenic microbes for possible antimicrobial effects. While antibacterial properties have been demonstrated with cicada wing nanostructures against *Pseudomonas aeruginosa,*[28-20] the biophysical mechanism remains unknown. Previous studies have shown cell ruptures demonstrated by a propidium iodide signal staining leakage of bacterial DNA.[24,28] In this thesis, we conduct antimicrobial effects of our bioinspired nanotopography in undisturbed growth media. We observe little rupture due to the absence of multiple media aspirations and surface washes that inflict stress on the cell membrane. We further investigate biophysical effects of antibacterial nanopillared surfaces with the approach of combining a materials science and engineering point of view with microbiology knowledge and a mechanobiological future outlook. Here, we ask: (1) Can bioinspired nanotopography hinder bacterial virulence, a biophysical effect resulting from surface-attachment? (2) Can bioinspired nanotopography disrupt bacterial motility, a mechanoresponsive ability resulting from surface sensing appendages? (3) Can bioinspired nanotopography inhibit filamentous fungi, a eukaryotic cell type that would provide a new antimicrobial system?

CHAPTER 2. Bioinspired Nanotopography Hinders *Pseudomonas aeruginosa* Virulence

Abstract

Nanostructured surfaces consisting of nanopillar arrays inspired by the lotus leaf, dragon fly and cicada wing, and gecko foot have inspired engineers to develop bioinspired nanotopography for inhibiting growth of bacteria. While cellular rupture mechanisms have been modelled and postulated, the influence of biophysical effects and microbial mechanobiology due to surface-attachment has have been overlooked. Here, we demonstrate the effect of bioinspired nanotopography in varying geometries on hindering biofilm formation of *Pseudomonas aeruginosa*. We then quantify the dependence of virulence on surface-attachment using an amoeba host killing assay with *Pseudomonas aeruginosa* PA14 wild-type and surface-attachment knockout mutants PilTU, FlgK, and PilTU-FlgK. We next analyzed the proton motive force activity followed by metabolic analysis using fluorescence lifetime imaging microscopy on flat and nanopillared surface structures. We found that bacterial cells on nanotopography exhibited a hindrance in virulence and proton motive force, which opens new perspectives in the biophysical effects of nanotopography.

Introduction

Previous studies have demonstrated and postulated cell rupture theories of antibacterial effects on bioinspired nanotopography against *Pseudomonas aeruginosa,*[28-30] yet biophysical effects and microbial mechanosensation have been overlooked. While microbial cells have often been modelled as rod shaped bags of enzymes, the complex biochemical processes and machinery[31-34] involved in proliferation and motility[35-37] have not been investigated on nanotopography in order to fully elucidate the latter's effect. To accomplish this goal, mechanobiology studies must be carried out to study the cell-surface attachment interaction at the nanoscale. Such studies have now been well established for eukaryotic cells including those on nanotopography.[38] In this work, we explore biophysical effects on antibacterial nanotopography that correspond with surface sensing, such as biofilm formation and virulence. This opens new doors to investigating how forces such as adhesion may influence virulence, a biophysical effects requiring surface attachment.

P. aeruginosa has been shown to exhibit virulence induced by surface attachment[39] likely due to the surface sensing of the membrane exposed PilY1 protein[40-42] and the production of the secondary messenger cyclic diguanylate monophosphate (c-di-GMP).[43,44] Effects of surface-attached virulence of *P. aeruginosa* have been demonstrated in assays against *Dictyostelium Discoideum* (amoebae)[45] as the virulence of *P. aeruginosa* largely depends on secreted toxins that can kill *D. Discoideum* cells[46-48] and reconstruction of the metabolic network.[49] We demonstrate in this thesis how bioinspired nanotopography with antibacterial properties can inhibit biofilm formation and further describe the extension of our studies to inhibiting virulence of surface-attached bacteria.

In 2011, Kralj, *et al*.[50] engineered an *Escherichia coli* strain with a proteorhodopsin optical proton sensor (PROPS) to obtain a bacteria fluorescence signal corresponding in intensity to the proton movie force activity. The PROPS membrane protein is designed to be a biological sensor for pH and proton transport by the proteorhodopsin requiring a retinal Schiff base pKa value of 9.6. The fluorescence signal strength correlates with the bacterium proton motive force, possibly due to the PROPS amino group facing the cytoplasm resulting in protonation.[50,51] Previous work has demonstrated that membrane tension induces growth arrest through electrical depolarization,[52-53] which may correspond with cellular proliferation.[54] Additionally, electrical signaling has been shown to attract bacterium to biofilms caused by membrane potential dependent modulation.[55] Such work has inspired our studies of analyzing PROPS cells on our bioinspired nanotopography to monitor changes in the proton gradient as a mechanism for inhibition in biofilm formation. We aimed to investigate the bacterial proton motive force, the energetic process that drives translocation of protons across the membrane, on nanotopography. This proton gradient is responsible for adenosine triphosphate (ATP) production, bioelectrical signaling, and motility in bacterial cells. We suspect that there exists an inhibition in this process on the nanotopography.

As a follow up investigation on biofilm formation hindrance, virulence hindrance, and proton motive force hindrance, we aim to investigate the metabolic activity of bacteria on nanotopography. Previous studies have demonstrated the use of fluorescence lifetime imaging microscopy (FLIM) in measuring the metabolic activity of nicotinamide adenine dinucleotide (NADH) fluorophores in antibiotic environments.[56,57] FLIM is a label-free, non-invasive, metabolic imaging technique that can measure the excited state decay rate of

fluorophores such as enzyme-bound NADH used here. FLIM analyzes the lifetime decay of each pixel acquired in each image through a Fourier transform to generate a phasor plot. In such a plot, the x-axis of the 2D histogram represents the cosine, whereas the y-axes represents the sine of the intensity. A semicircular area then forms spanning from G=0-1 and S=0-0.5, representing two phasor vectors, which indicate a lifetime map of fluorescent intensities. The left shifted histograms indicate a low ratio of free to bound NADH, while the right shifted histograms indicate a high ratio of free to bound NADH.[58,59] Here, we study the growth inhibition of *P. aeruginosa* on nanotopography and the resulting hindrance of virulence, proton motive force, and metabolism.

Results and Discussion

P. aeruginosa cells were grown in single well imaging dishes with PMMA flat, C200, P300, and P500 bottom surfaces (**Table 1**) in Peptone S medium and development buffer (PS:DB) medium at 37^{o}C to assess their biofilm inhibiting properties (**Figure 4**). Each imaging dish was then loaded on an Eclipse Ti inverted research microscope so phase images of surface-attached cell growth could be taken at each timepoint. While biofilm formed on each surface after eight hours, the growth process was hindered most on the C200 surfaces followed by the P300 and P500 surfaces. In contrast, *Vibrio cholerae* cells grown in similar conditions, exhibited a greater surface growth on nanotopography than the flat surfaces. (**Figure 5**). Gram-negative *V. cholerae* was tested as it is an additional highly pathogenic strain of global healthcare concerns,[60] yet exhibits a curved cell body shape due to periplasmic CrvA self-assembled polymers[61] and possesses unique mechanosensors for selective advantage.[62-64]

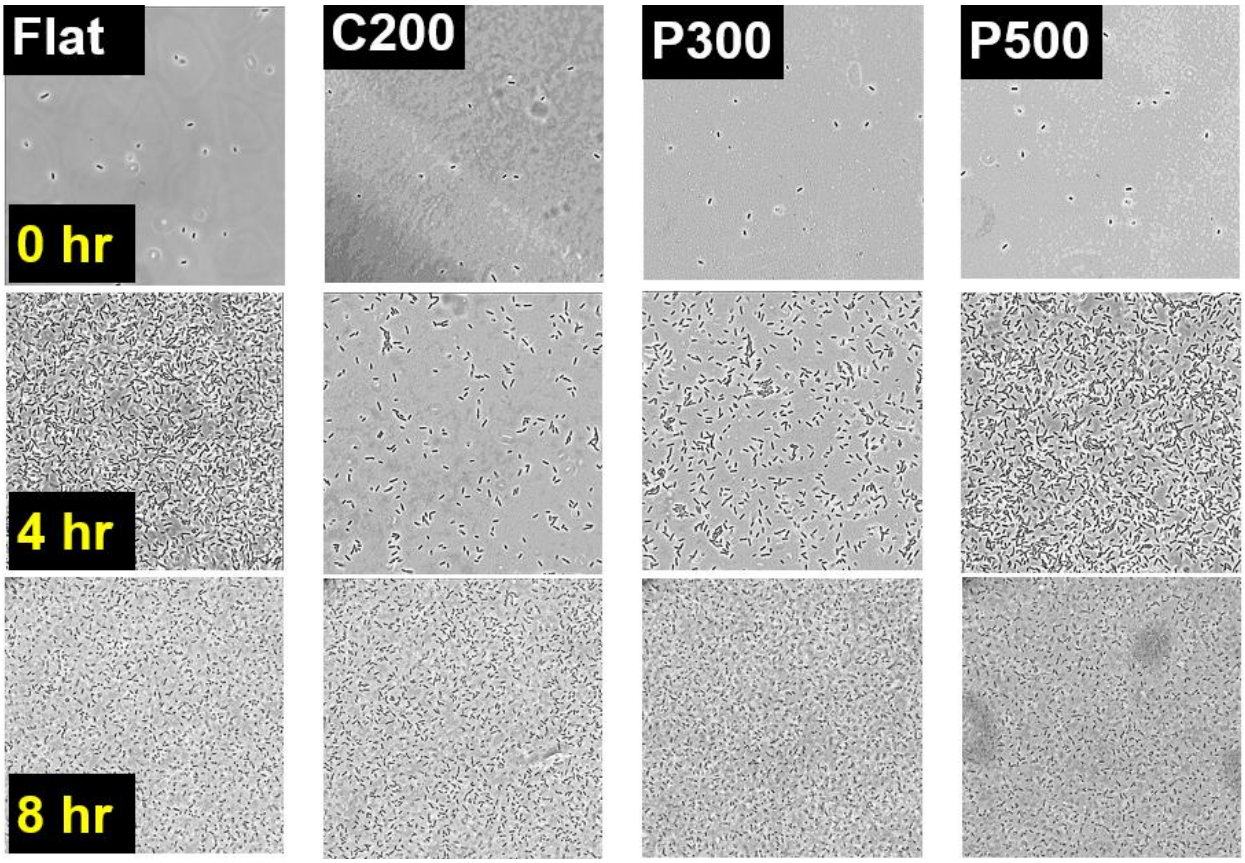

Figure 4. Nanotopography hindered *P. aeruginosa* biofilm formation. Phase images were taken after 30 minutes of surface attachment followed by 4 hours of incubation at 37°C. The C200 surface followed by the P300 and P500 surfaces exhibited the greatest inhibition in growth. After 8 hours, biofilm formed on all surfaces.

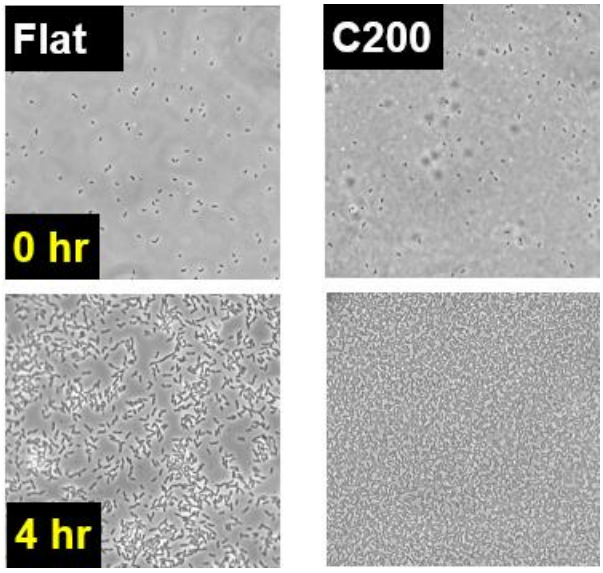

Figure 5. Nanotopography encouraged *V. cholerae* biofilm formation after 4 hours of incubation at 37°C.

Scanning electron micrographs were taken to analyze the cell-surface interaction of *P. aeruginosa* and *V. cholerae* with the nanopillars. Cells were fixed with 4% paraformaldehyde and dehydrated in serial ethanol dilutions to prepare samples for 5nm iridium sputter coating suitable for SEM analysis. Both cell types exhibited surface-attachments on the nanopillars without cellular rupture or leakage (**Figure 6**). The intact cells are contrary to and add to previous studies of *P. aeruginosa* on nanotopography possibly due to the elimination of medium aspirations and washing of the surfaces that could inflict stress and rupturing of cells on nanotopography. While both surface-attached cell types exhibit different cell shapes for unique competitive advantages in nature, other surface-attachment factors such differences in pili machinery and gene expression may play a role in growth inhibition or promotion on nanotopography. This work presents an example of gram-negative bacteria to avoid in growth inhibition applications.

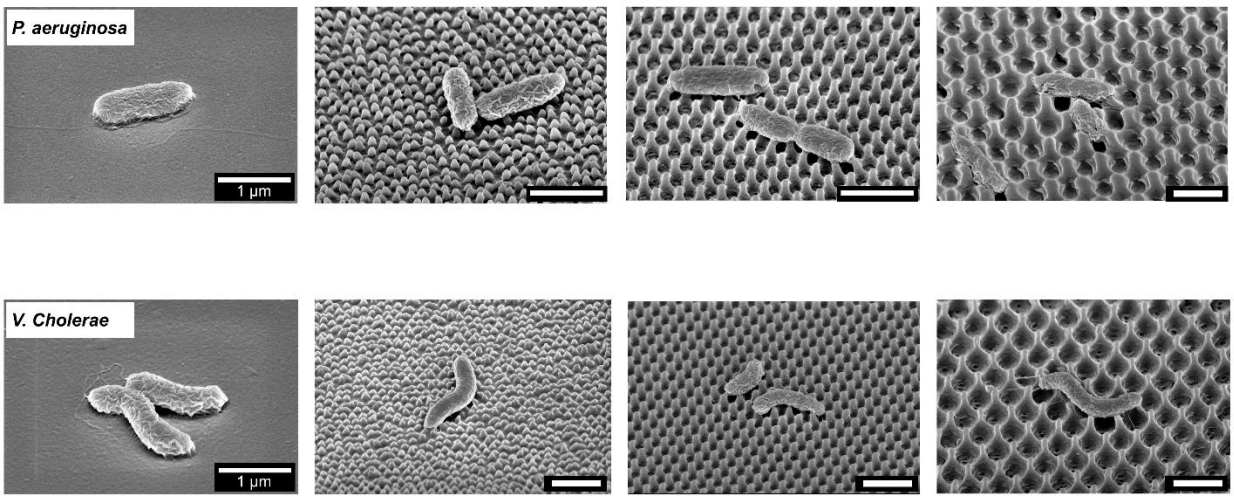

Figure 6. SEMs of *P. aeruginosa* and *V. cholerae* flat and on nanotopography. Cells exhibited surface attachment to nanopillars and did not exhibit rupturing.

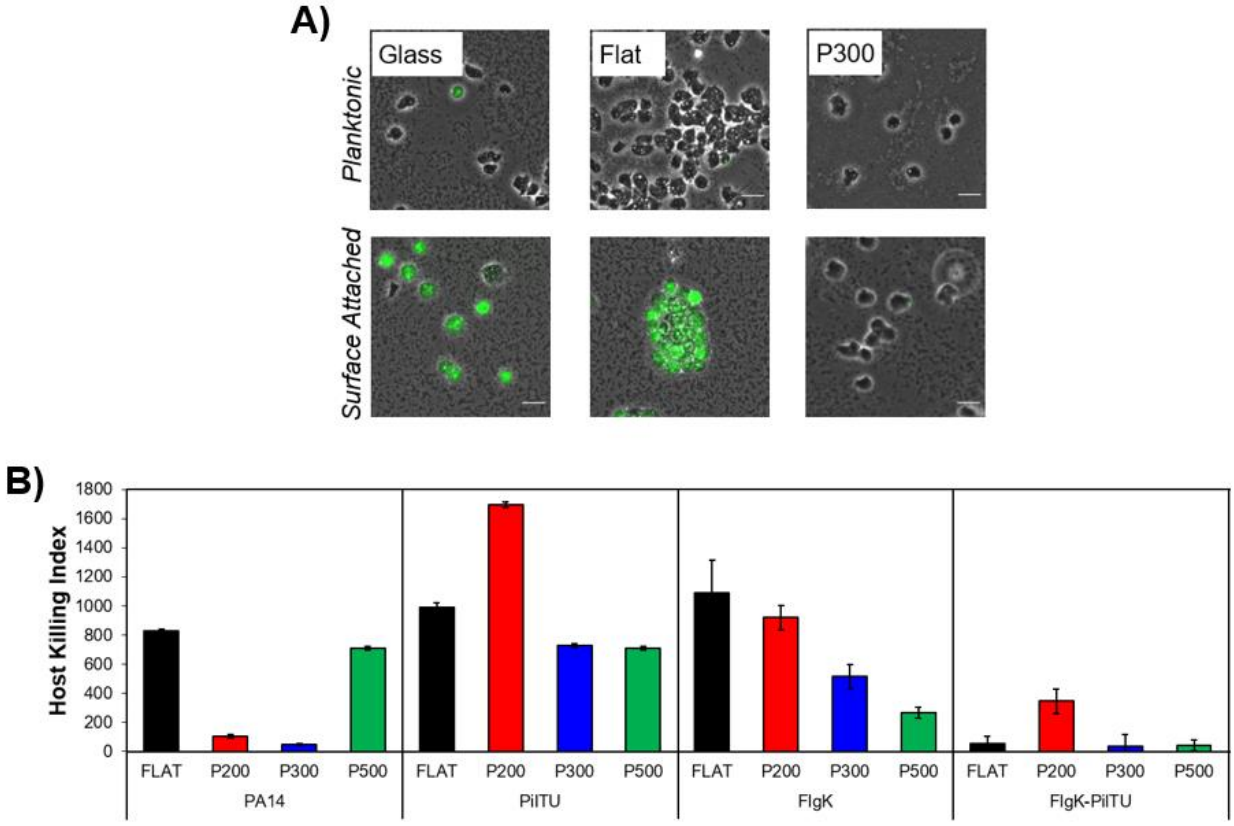

Figure 7. Nanotopography hindered *P. aeruginosa* virulence. (a) Composite phase images of planktonic and surface-attached *P. aeruginosa.* When *P. aeruginosa* becomes surface-attached, the virulence is activated and toxins are secreted to kill host and rupturing of *D. Discoideum* (amoeba) as shown with calcein-AM fluorescence (green). (B) The y-axis represents host killing index, while the x-axis represent PA14 and knockout mutants. The host killing index was hindered on nanotopography and most prevalent in PA14.

PA14 wild type or knock out mutants PilTU, FlgK, and FlgK-PilTU were individually grown on flat, C200, P300, and P500 surfaces in PS:DB medium at 37°C for eight hours and co-cultured with *D. Discoideum* (amoebae) in methods previously described[45] to assess hindrance in surface-attached virulence. The PA14 cells exhibited the greatest hindrance in virulence, whereas the PilTU and FlgK mutants lacking PilTU pili retraction motors and flagellar exhibited less hindrance in virulence, while PilTU-FlgK mutant exhibited no inhibition at all (**Figure 7**). Such mutants lack surface sensing and motility appendage functionality, which may contribute to the underlying mechanism of virulence hindrance.

E. coli strain BW25113 with a genetically engineered proteorhodopsin optical proton sensor (PROPS)[50,51] was used to evaluate possible inhibition of the gram-negative, rod-shaped bacterium on the flat, C200, P300, and P500 surfaces (**Figure 8**). A stronger fluorescence signal is correlated with an inhibited proton motive force. The *E. coli* cells exhibited a greater inhibition in proton motive force after 1 hour of incubation on the C200 surfaces followed by the P500 and P300 surfaces indicating the nanotopography may have bacterial proton gradient inhibition effects (**Figure 8**). A proton motive force hindrance would correspond to inhibition in surface sensing, motility, bioelectrical communication amoungst cells, and ATP generation.

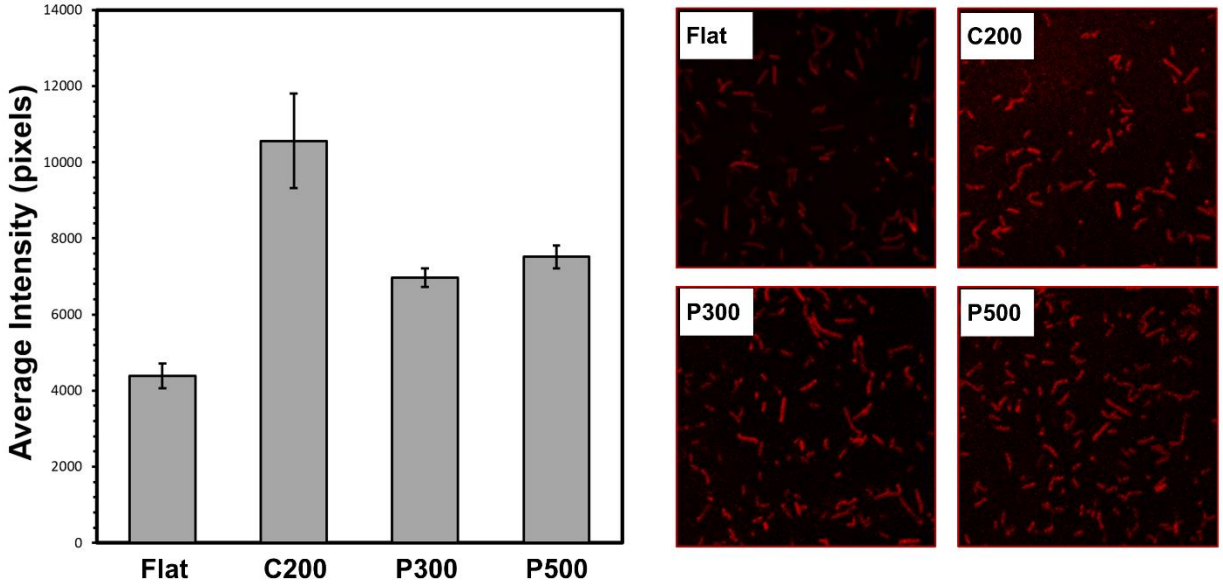

Figure 8. Nanotopography hindered *E. coli* proton motive force. The greatest inhibition was exhibited on the C200 surfaces with close inhibition on the P300 and P500 surfaces.

We hypothesized that hindrance in biofilm formation, virulence, and proton motive force may result in decreased activity of NADH during cellular metabolism. We used FLIM to measure the metabolic activity of PA14 wild type and knock out mutants PilTU, FlgK, and

FlgK-PilTU on the flat, C200, P300, and P500 surfaces (**Figure 9**). There was no statistically significant trend in free to bound NADH results indicating that NADH activity during metabolism does not play a significant factor in the antibacterial properties of bioinspired nanotopography C200, P300, or P500. The C200 surfaces showed consistent shift in metabolism of decreased free to bound NADH, which may indicate a boost in metabolism to compensate for virulence and proton motive force hindrance, yet more studies must be conducted.

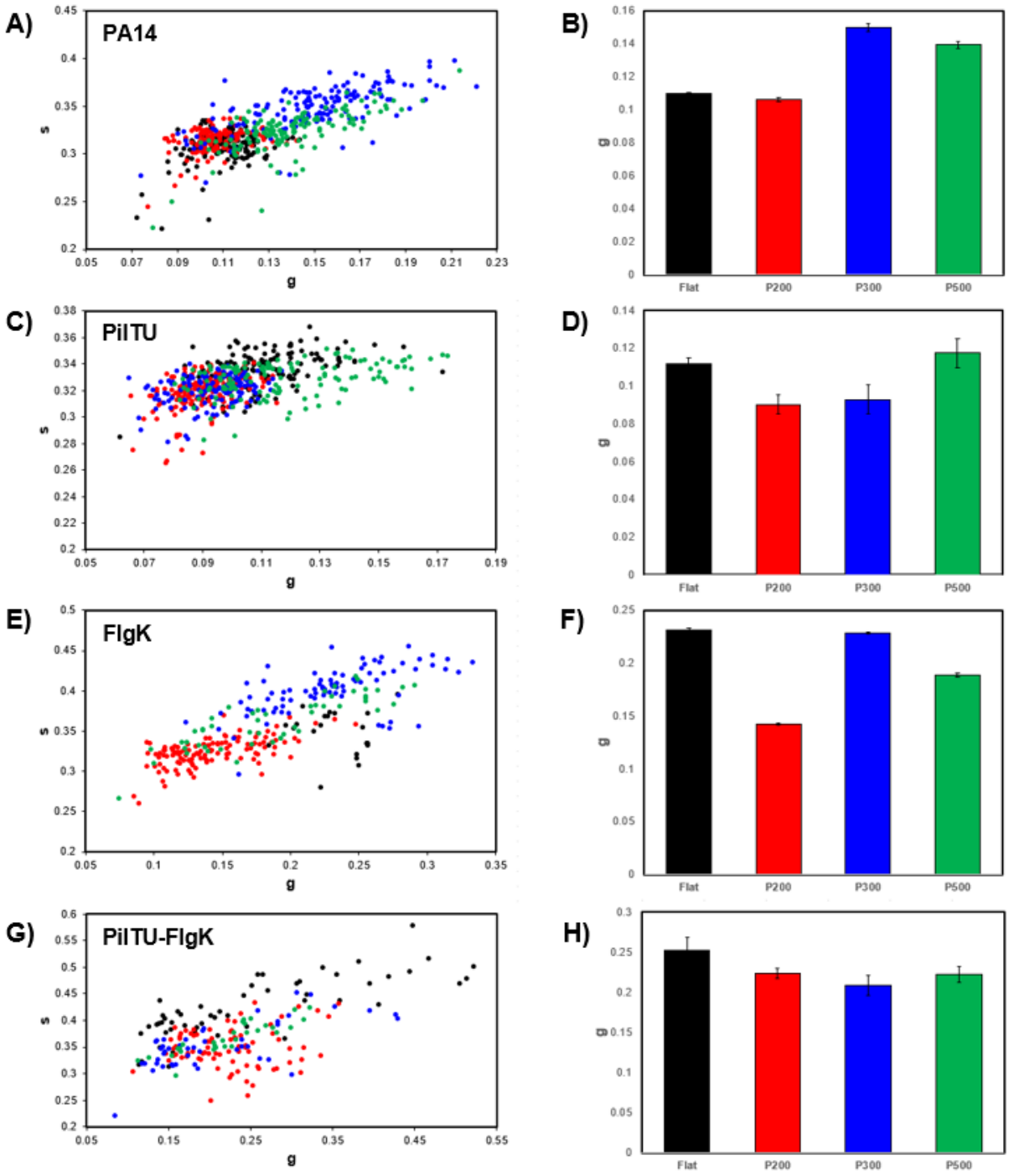

Figure 9. Fluorescence lifetime imaging microscopy (FLIM) of *P. aeruginosa* free to bound NADH on nanotopography. Cells on the C200 surfaces exhibited a lower ratio of free to bound NADH, while the P300 and P500 surfaces showed no statistically significant trend.

Experimental Methods

Bacterial Growth Conditions. *P. aeruginosa* strains PA14 wild-type, PilTU, FlgK, and FlgK-PilTU along with *Vibrio cholerae* wild-type were streaked on Luria-broth/Miller (LB) Petri dishes from frozen stocks using a sterile loop method and incubated for 16 hours at 37^{o}C. Single colonies were each then inoculated in 3mL of PS:DB media and placed on a rotating incubator for 16 hours at 37^{o}C.

Bacterial Growth Microscopy. Overnight cultures were back-diluted to reach a mid-log optical density of 0.3 at 600 nm (OD_{600}). Then, 3mL of PS:DB media was pipetted into each glass bottom dish containing flat or nanopillared PMMA bottom surfaces. Next, 30μL of each strain was then inoculated onto each flat or nanopillared PMMA surface allowing 30 minutes of surface attachment. Following, each imaging dish was immediately loaded on an Eclipse Ti inverted research microscope (Nikon, Melville, NY) with NIS-Element software and imaged using a 100x oil objective at room temperature. All imaging dishes were incubated at 37^{o}C between each imaging timepoint.

Bacterial Scanning Electron Microscopy. After each bacterial growth analysis, the PS:DB broth in each imaging dish was slowly aspirated out and replaced with 2mL of 4% paraformaldehyde (PFA) for 20 minutes to allow fixation of surface-attached cells. Then, the PFA was slowly aspirated out and replaced with 50% ethanol in DI water for 15 minutes. A series of 15-minute serial dilutions followed with 70%, 80%, 90%, 95%, and 100% ethanol in DI water for each surface for completed dehydration of the surface-attached cells. Cells were left in a fume hood overnight to fully dry before being coated with 5nm of iridium, using an ACE600 sputter coater (Leica Microsystems, Buffalo Grove, IL) to provide a conductive coating suitable for scanning electron microscopy imaging. The

surface-attached cells on each surface were then characterized using a FEI Magellan 400 XHR Scanning Electron Microscope (FEI Company, Hillsboro, OR) at a 45° tilt angle and an acceleration voltage of 3 kV.

***Pseudomonas aeruginosa* Virulence Assay.** *D. Discoideum* (amoebae) was grown and co-cultured with PA14 wild type or knock out mutants PilTU, FlgK, and FlgK-PilTU using a rapid image-based virulence assay previously described.[45] Each *P. aeruginosa* cell type was grown on flat, C200, P300, or P500 triplicate surfaces at 37°C for eight hours

***Escherichia coli* Proton Motive Force Assay.** *E. coli* strain BW25113 (Δ(araD-araB)567, ΔlacZ4787(::rrnB-3), lambda-, rph-1, Δ(rhaDrhaB)568, hsdR514) with proteorhodopsin optical proton sensor (PROPS) plasmid pJMK0001 (pBAD vector with RPOPS, AmpR) was streaked on Luria-broth/Miller (LB) Petri dishes with 100μg/mL Amp from frozen stocks using a sterile loop method and incubated for 16 hours at 37°C. Single colonies were each then inoculated in 5mL of LB and 5μL of 100μg/mL Amp in a culture tube incubated shaking at 33°C for 16 hours. Cultures were back diluted to a starting OD_{600} of 0.05 and incubated in 50mL LB with 50μL of 100μg/mL Amp shaking at 33°C until they reached an early-log phase with an OD_{600} of 0.3-0.4. Then, 50μL of arabinose inducer and 12.5μL of all-*trans* retinal was added to each culture and incubated shaking for 3.5 hours at 33°C in the dark. Cells were next harvested by spinning in a JA20 rotor at 6000rpm for 15 minutes before washed with and resuspended in 1XM9 minimal medium.

Cultures were back-diluted to reach a mid-log optical density of 0.3 at 600 nm (OD_{600}). Then, 3mL of M9 was pipetted into each glass bottom dish containing flat or nanopillared PMMA bottom surfaces. Next, 30μL of each strain was then inoculated onto each flat or nanopillared PMMA surface allowing 30 minutes of surface attachment.

Following, each imaging dish was loaded on a Zeiss LDM710 confocal microscope after 1 hour of incubation with a 561nm solid state excitation laser and imaged using a 63x oil objective at room temperature.

Fluorescence Lifetime Imaging Microscopy (FLIM). PA14 wild type and knock out mutants PilTU, FlgK, and FlgK-PilTU were grown on the flat, C200, P300, and P500 surfaces in PS:DB medium at 37^{o}C for eight hours before analyzing the surface effects on metabolism. FLIM was conducted using a multiphoton microscope on an Olympus FV1000 system and Olympic IX81 microscope with an excitation at 740nm and a 63X oil objective. Data were analyzed using SimFCS software (LFD, UCI) and calibrated using Rhodamine 110 with a known lifetime of 4 ns.

Conclusions and Future Outlook

In conclusion, we demonstrated that our bioinspired nanotopography hindered surface sensitive bacterial properties. Biofilm formation of *P. aeruginosa* was found to be hindered most on the C200 surfaces, followed by the P300 and then P500 surfaces. Additionally, the host killing index of surface-attached *P. aeruginosa* decreased significantly on the nanotopography for PA14 wild type cell and slightly for the PilTU and FlgK mutants lacking surface sensing and motility appendages. These results may indicate motility on surface-attached cells may lead to virulence and/or growth inhibition due to stress on the membrane. Additionally, initial surface sensing may contribute to the hindrance in biofilm formation. The proton motive force in *E. coli*, responsible for motility, cellular communication, and ATP generation, was also hindered on the nanotopography with the highest inhibition on the C200 surfaces consistant with our hypothesis. Future work

remains in developing a proton gradient sensing assay for other bacterial strains such as *P. aeruginosa.* While the *P. aeruginosa* metabolism was analyzed by measuring the NADH activity using FLIM, there was no significant shift in metabolic activity of NADH among the nanopillared surfaces. Future studies could investigate ATP production, a result of proton motive force activity, of *P. aeruginosa* and other bacterium on bioinspired nanotopography using Föster resonance energy transfer sensors.[65] Many further questions remain. For instance, what role do surface surface-attachment pili play such as the fimbriae? We must also ask, what role does the pilY1 protein play when virulence is decreased on nanotopography? Yet another investigation would be to ask if quorum sensing is inhibited on the bioinspired nanotopography, which when inhibited, blocks *P. aeruginosa* virulence.[66]

CHAPTER 3. Bioinspired Nanotopography Disrupts *Pseudomonas aeruginosa* Mechanoresponsive Upstream Motility

Abstract

Pseudomonas aeruginosa is an opportunistic, multidrug-resistant, human pathogen that forms biofilms in environments with fluid flow, such as the lungs of cystic fibrosis patients, industrial pipelines, and medical devices. *P. aeruginosa* twitches upstream on surfaces by the cyclic extension and retraction of its mechanoresponsive type IV pili motility appendages. The prevention of upstream motility, host invasion, and infectious biofilm formation in fluid flow systems remains an unmet challenge. Here, we describe the design and application of scalable nanopillared surface structures fabricated using nanoimprint lithography that reduce upstream motility and colonization by *P. aeruginosa*. We used flow channels to induce shear stress typically found in catheter tubes and microscopy analysis to investigate the impact of nanopillared surfaces with different packing fractions on upstream motility trajectory, displacement, velocity, and surface attachment. We found that densely packed, subcellular nanopillared surfaces, with pillar periodicities ranging from 200 to 600 nm and widths ranging from 70 to 215 nm, inhibit the mechanoresponsive upstream motility and surface attachment. This bacteria-nanostructured surface interface effect allows us to tailor surfaces with specific nanopillared geometries for disrupting cell motility and attachment in fluid flow systems.

Introduction

Bacteria in nature have often been found to colonize and form biofilms in environments with fluid flow such as the vasculatures of plants,[67] the lungs of cystic fibrosis patients,[68] and aquatic environments since their appearance in fossil records dating back to 3.25 billion years.[14] Biofilm formation is problematic in industrial and health-care systems such as fuel lines in aviation,[69] naval hulls,[70] conduits and storage tanks for potable water,[71] and medical devices.[1]Biofilms consist of surface-attached cells protected by layers of secreted extracellular polymeric substances, which are key factors for cell survival in diverse environments.[14] In health care, biofilms promote a 10- to 1000-fold decrease in the diffusion of antibacterial drugs from outside the biofilm and may alter bacterial gene expression,[11,12, 72] resulting in antimicrobial resistance.[73] Human pathogenic biofilms are responsible for 80% of clinical infections, leading to 1.7 million hospital-acquired infections and 99 000 annual deaths[2] with treatments costing 16.6 billion dollars annually in the US alone.[3] There is an urgent need to prevent the proliferation of infectious bacteria on surfaces without the use of drugs that could lead to antimicrobial resistance.

Antimicrobial resistant, Gram-negative bacteria often persist in environments with fluid flow with the aid of mechanoresponsive motility mechanisms such as those possessed by human pathogenic *Vibrio cholera*,[74] *Neisseria gonorrhoeae*,[75] *Escherichia coli*,[76] and *Pseudomonas aeruginosa*.[35] In this work, we focus on *P. aeruginosa*, a biofilm-forming, opportunistic pathogen known to cause chronic infections in immunocompetent and immunocompromised patients. *P. aeruginosa* ubiquitously contaminates medical implants and devices with fluid flow such as mechanical ventilators,[77] prosthetic heart valves,[5] and catheters.[8] *P. aeruginosa* forms biofilms through cell-to-cell communication, or

quorum sensing, between surface-attached cells through regulated gene expression in response to changes in population density.[13]

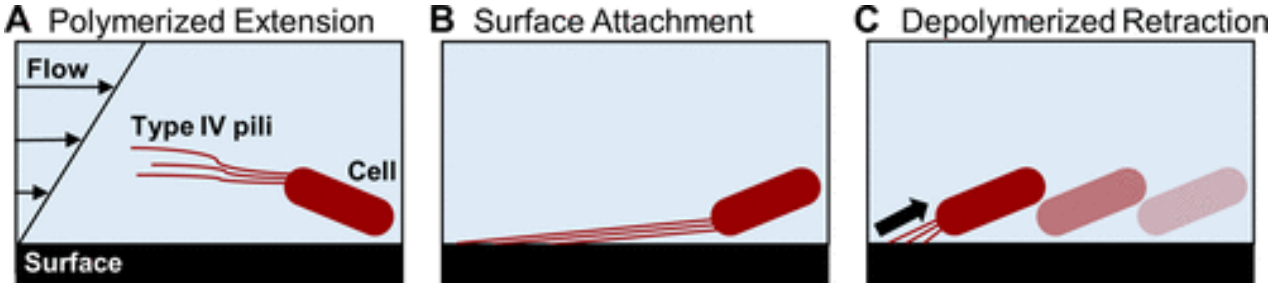

Figure 10. Schematic of type IV pili-mediated upstream motility on surfaces. *P. aeruginosa* activates mechanoresponsive motors to facilitate type IV pili cyclic sequence of (A) polymerized extension, (B) surface attachment, and (C) depolymerized retraction to generate an upward driving force.

Surface attachment in environments with fluid flow is facilitated in *P. aeruginosa* through the activation of its type IV pili, a mechanoresponsive motility mechanism.[35] Type IV pili are flagellum-independent, filamentous appendages for motility and translocation, which were first discovered in 1961.[78] These appendages mediate surface adhesion and enable *P. aeruginosa* to twitch[74,79,80] and slingshot[81] upstream by the cyclic sequence of polymerized extension, surface attachment, and depolymerized retraction[82-87] (**Figure 10**). These motions are facilitated by the activity of the PilT and PilU ATPase motors,[88] which generate an upstream driving force and are regulated by the Chp chemosensory system.[89] Type IV pili are distributed radially at the cell poles and have been measured to be 7–20 nm in diameter and several microns in length using optical tweezers,[90] total internal reflection microscopy with fluorescently labeled cells on a quartz slide adhered to a silica prism,[91] and interferometric scattering microscopy.[92] Pili have been characterized as the strongest linear molecular motors to date and are able to produce 100–250 pN of shear force.[85,93,94]

Previous studies have observed *P. aeruginosa* in flow channels with flat glass surfaces under varied flow rates and shear stresses ranging from 0.1 to 10 Pa.[88] Using single and multibranched channels, previous work observed rheotaxis, colonization, and upstream migration on surfaces under varying flow rates and shear stresses.[88,95] Along with serving as appendages for motility, type IV pili are important virulence factors during the early stages of infection[96-98] and they mechanochemically mediate the activation of virulence when cells are surface-attached,[95] leading to the formation of virulent biofilms.[35,96,98-100]

Previous work has demonstrated that surfaces with hemispherical topographies on the microscale with features of several magnitudes larger in diameter than the cellular bodies can hinder *P. aeruginosa* net motility, yet motility in relation to flow direction and surface detachment was not observed.[101] Although microtopographies have shown promise in prolonging biofilm formation by confining the cell motility in grooves between hemispheres, the use of subcellular nanotopography may, by contrast, disrupt its adhesive type IV pili mechanoresponsiveness. This would prevent *P. aeruginosa* surface adhesion from outcompeting the force of the flow. This phenomenon would inhibit both motility and surface attachment in environments where the shear stresses from fluid flow could trigger rheotactic upstream motility. The use of biomimetic, nanopillared surfaces inspired by those found on lotus leaves (*Nelumbo nucifera*),[17] gecko feet (*Gekkonidae*),[19] and cicada wings (*Psaltoda claripennis*)[24,28] has been promising for antibacterial medical device coatings. However, their antimicrobial properties have only been investigated in static fluid environments.[102] The effectiveness of such engineered surfaces in environments with fluid flow needs to be demonstrated.

In this work, we extend the use of bioinspired, nanopillared surfaces in fluid flow for the purpose of disrupting both upstream surface motility and attachment of *P. aeruginosa*. We demonstrate a new strategy of surface structuring a medical device material, poly(methyl methacrylate) (PMMA), without any chemical modification or addition of antibiotics. We used nanoimprint lithography (NIL), a low-cost and scalable topography engineering technique to fabricate surfaces of nanopillars with varying packing fractions. The viability of NIL has already been shown in the semiconductor industry for the manufacture of high-density circuits.[24,103] During fluid flow, these nanopillared surfaces have been reported to possess hydrophobic properties at the nanometer length scale with minimal increased slip length, b, due to zero slip (b = 0) at the solid–liquid interface and perfect slip (b = infinity) at the liquid–vapor interfaces.[104,105] Although such properties have been caused by nanobubbles reducing the drag in water,[106] such nanobubbles have been found to decrease over a period of an hour, resulting in zero slip.[107] Here, we found that degrees of surface hydrophobicity did not correlate with motility trends. Thus, we can assume that small changes in fluid flow insignificantly affect bacterial surface motility.

Furthermore, we analyzed the motility data of *P. aeruginosa* in relationship to the decreased surface area that the type IV pili contact due to varying packing fractions of the subcellular nanopillars on the surfaces. Herein, we present our results on quantifying the following behavior of the cells: upstream trajectory, displacement, velocity, angular trajectory, and persistent surface attachment on flat PMMA surfaces compared to those on nanopillared PMMA surfaces. These phenomena at the interface of bacteria nanotopography allow us to tailor surfaces with specific nanopillared geometries for structurally disrupting mechanoresponses, signal transduction, and motility in fluid flow.

Our findings are relevant to antibacterial, antivirulent, and antibiofilm design strategies for preventing contamination in industrial and medical device applications such as catheters.

Results and Discussion

We fabricated nanopillared surfaces on PMMA, an FDA-approved polymer commonly used on medical devices (**Figure 3**). NIL[24,25] was used to fabricate uniform arrays of nanopillars that ranged in center-to-center pillar periodicities of 200, 300, 500, and 600 nm. The letterings for C200, P300, P500, and P600 represent the negative imprinting mold originating from a cicada wing or pillared master mold, whereas the numeric values in the nomenclature represent nanometer center-to-center pillar periodicities per surface (**Table 1**). For the present case, we identified the pillar tip packing fractions, Φ, as the ratio of the pillar tip surface area to the substrate surface area in decreasing order from P300, P600, C200, to P500 (**Table 1**).

We next analyzed *P. aeruginosa* motility in flow cells with flat or nanopillared PMMA as the bottom surface. We fabricated the flow cells by cutting out channels in a double-sided adhesive tape and capping the channel tops using a poly(dimethylsiloxane) (PDMS) block with precut inlet and outlet holes. The PDMS block placed on top of the adhesive tape on the PMMA surfaces allowed us to avoid having to use plasma bonding that may result in etching the nanopillars. The cross sections of the flow channels were 1 mm in width and 100 μm in height. These flow cells were then mounted atop an inverted microscope

(**Figure 11A**), and phase images were taken every minute at room temperature to create time-lapse videos of the *P. aeruginosa* motility (**Figure 11B**).

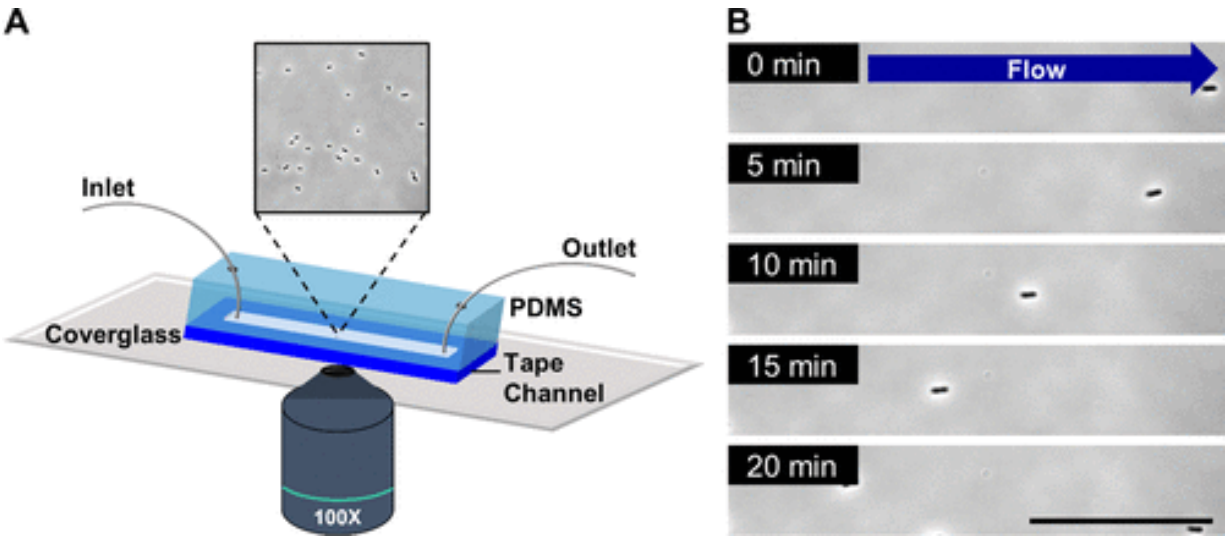

Figure 11. Continuous surface-attached cell motility imaging system. (A) Schematic of flow cell loaded with *P. aeruginosa* mounted on an inverted microscope and imaged through a 100× oil objective. Once cells were surface-attached, only fresh lysogeny broth (LB) media flowed through the inlet at 115 μm/min. The cross sections of the channels were 1 mm wide and 100 μm tall (shear stress of ~1 Pa). (B) Time-lapse demonstration of *P. aeruginosa* on a flat PMMA-coated surface exhibiting upstream motility. Scale bars represent 20 μm.

To demonstrate the effect of nanopillared surfaces on bacterial upstream motility, overnight *P. aeruginosa* cultures were diluted and grown to a mid-exponential phase to an optical density of 0.2 at 600 nm (OD_{600}) and seeded into each flow cell. Previous studies demonstrated that *P. aeruginosa* upstream motility was enabled by their mechanoresponsive type IV pili on glass surfaces at various flow rates ranging from 0.5 to 30 μL/min and shear stresses ranging from 0.1 to 10 Pa.[88,95] In this work, we applied a flow rate of 115 μm/min using lysogeny broth (LB) media on each flow cell to induce a shear stress of ~1 Pa on the seeded *P. aeruginosa* cells, a value typically found in catheter tubes.[108] We constructed plots from the time-lapse videos by tracking the motion of each

cell, normalizing their starting position, and quantifying their relative directions. In plots where we show the constructed trajectory, the cells that migrated from the origin 0 and extended to the negative *x*-axis direction indicate upstream translocation (**Figure 12**). The cells on the flat surfaces shifted largely in the negative direction on the *x*-axis compared to cells on the nanopillared surfaces. We demonstrated a correlation between surface nanostructucturing and motility inhibition in the results below.

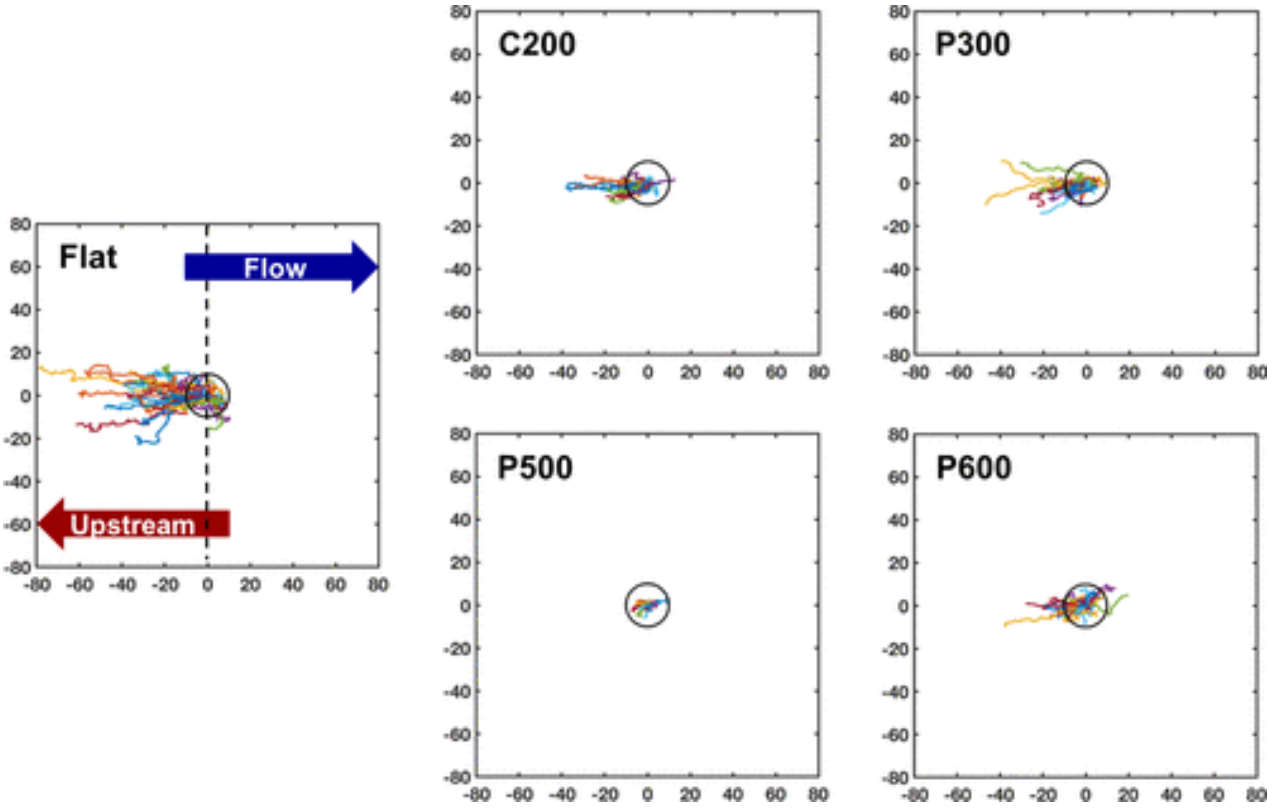

Figure 12. Single cell trajectories of *P. aeruginosa* motility on the flat and nanopillared surface structures. *n* = 50 for each surface. *x*-Axis and *y*-axis span from −80 to 80 μm. Trajectories originating from 0 and extending to the −80 μm *x*-direction indicated upstream motility. A ring with a radius of 10 μm is given for reference.

We quantified cell motility behavior on the flat and nanopillared surfaces to analyze the influence of nanopillared surface tip packing fraction, Φ, on motility inhibition. We

found that 30–90% of *P. aeruginosa* cells seeded into the flow cells with nanopillared bottom surfaces did not migrate upstream compared to those on the flat surfaces. The loss of migration on the surfaces was dependent on the nanopillar packing fractions (**Figure 13A**). On these nanopillared surfaces, 20–80% of *P. aeruginosa* cells exhibited a lower upstream velocity compared to those on the flat surfaces. The average upstream velocity of the cells on the flat PMMA surface was ~1.5 μm/min, which is consistent with the previous studies on flat glass surfaces.[88,95] The cells on P300 showed high resistance to motility followed by P600, C200, and P500 (**Figure 13B**). This trend correlated to the decreasing packing fraction at the top of the nanopillar arrays (**Table 1**). The reduction in the surface area at the pillar tips may have limited surface sensing, mechanoresponse, and attachment of the type IV pili, which resulted in the force of flow overcoming the force of adhesion (**Figure 13C**). Although there may have been an increase in slip on the nanostructured surfaces in molecular orders of magnitude,[104] our results did not correlate to the degrees of apparent hydrophobicity, θ (**Table 1**).

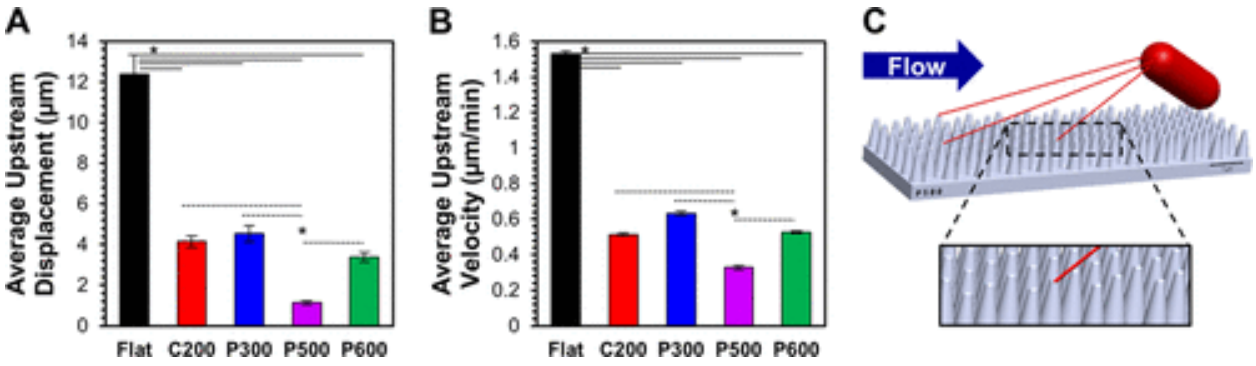

Figure 13. Nanopillared surfaces inhibited the upstream motility of *P. aeruginosa*. Data were collected from 2 h time-lapse videos using an ImageJ TrackMate plugin.[109] $n = 50$ for each surface. Experiments were performed in triplicates of each surface. (A) Average upstream displacement of cells. (B) Average upstream velocity of cells. The decreasing upstream velocity values corresponded to the reduction in pillar tip packing fraction, Φ. Error bars represent the standard error of the mean with statistical significance assessed using Student's *t* test. *: $p < 0.05$. (C) Schematic rendering of *P. aeruginosa* type IV pili adhesion to the nanopillared surface structures in fluid flow.

To further investigate the influence of reduced type IV pili surface contact area to upstream cell motility disruption, we measured the angular trajectories of the cells to monitor the degree of explored surface area compared to flow direction. Previous reports show that a zig-zag motion was observed during the upstream motion of *P. aeruginosa* on glass surfaces.[81,88,95] In this work, the orientation angle of each cell was measured with respect to the direction of flow (**Figure 14A**). The motility trajectories of the cells were compared among the surfaces with orientation angle with respect to the upstream direction recorded every minute for 1 h (**Figure 14B**). The average orientation angle of upstream motility was collected fromq five individual cells on each surface-attached for an hour and plotted as a histogram (**Figure 14C**). We found that the average orientation angles of motility increased as follows: 15.1 ± 1.6° for flat, 16.6 ± 1.7° for P600, 18.7 ± 2.4° for P300, 20.2 ± 2.2° for C200, and 25.8 ± 2.5° for P500. The increase in orientation angle correlated inversely with the decreasing packing fractions at the top of the nanopillar arrays (**Table 1**). We postulate that the larger orientation angles are due to the lack of attachable surface area at the top of the nanopillar arrays, which constrains the locations to which the type IV pili attach. Further studies imaging the type IV pili on the nanopillared surfaces in fluid flow would verify the postulation.

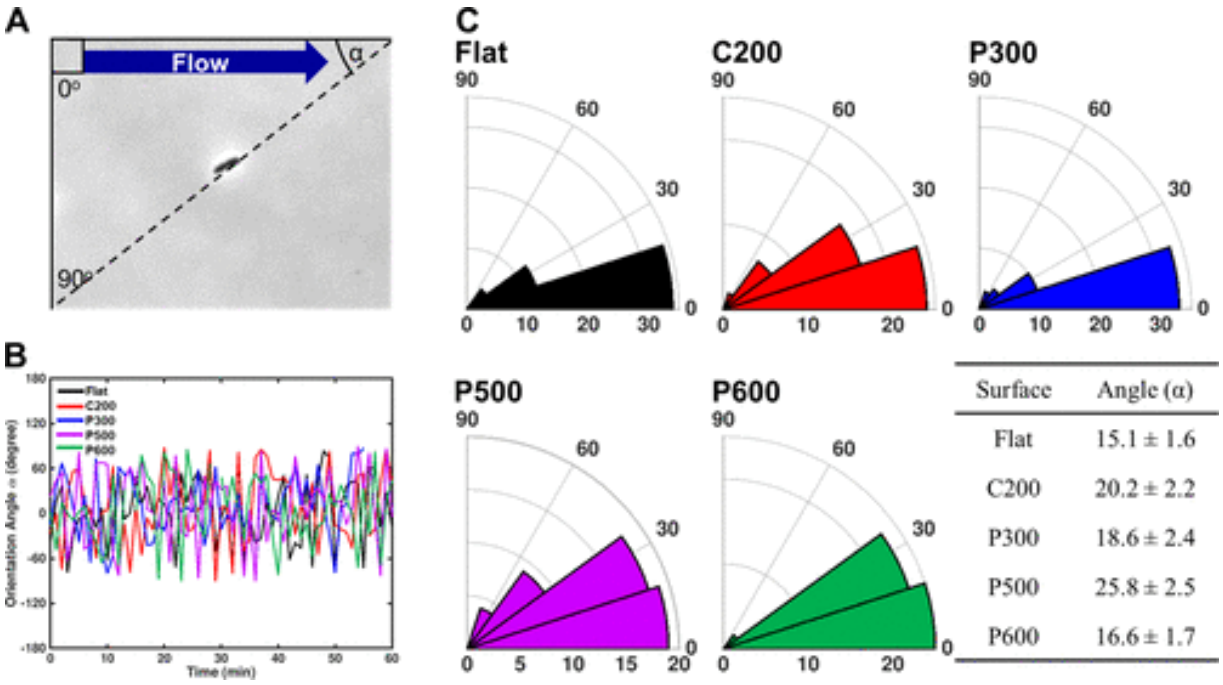

Figure 14. Angular trajectories of *P. aeruginosa* motility on the flat and nanopillared surface structures. (A) Schematic of cell orientation angle, α, measured in reference to the fluid flow direction. (B) Time lapse of angular cell trajectories was taken each minute for 1 h on all surfaces. (C) Angular trajectory histograms of cells on flat, C200, P300, P500, and P600. *n* = 5 for each surface. The larger average orientation angles on the nanopillared surfaces may indicate that the *P. aeruginosa* type IV pili explored larger areas to adhere to than on the flat surface. Standard deviations are given for each average orientation angle per surface.

The shear stress from fluid flow that accompanies increased surface motility, cell proliferation, and residence time[110] in *P. aeruginosa* produces signaling precursors for infectious biofilm formation.[76,84,96,100] Although the nanopillared surfaces inhibited upstream displacement and velocity of *P. aeruginosa*, we further measured whether the surfaces reduced surface attachment for long-term antifouling applications. Here, we recorded the percentage of cells on each surface every minute for 2 h in the same flow channels while simultaneously analyzing the cell displacements, velocities, and trajectories. The data shown in the graph display an average of triplicate surface measurements at each minute. On the flat PMMA surfaces, the cells divided and proliferated over the 2 h course. On the nanopillared surfaces, the overall population of the cells decreased due to

detachment over a period of 2 h (**Figure 15A**). Although the increasing detachment did not directly correlate with the reduction in surface area at the top of the nanopillar arrays that the type IV pili would sense, still, these observations demonstrate that surface attachment inhibition on reduced surface areas in fluid flow played a significant role.

Although all nanopillared surfaces showed reduction in cell division and surface attachment, this effect can be most clearly observed on the P500 surface compared to that on the flat surface (**Figure 15B**). The study presented here provides a general technique using surface nanopatterning to avoid biofouling in fluid flow environments by systematically altering the surface using nanoimprinting. Our findings also hold significance in using nanostructured surfaces to both understand the biophysical mechanism of mechanoresponsive type IV pili in fluid flow and further investigate drug-free, antivirulent, and antibiofilm coatings.

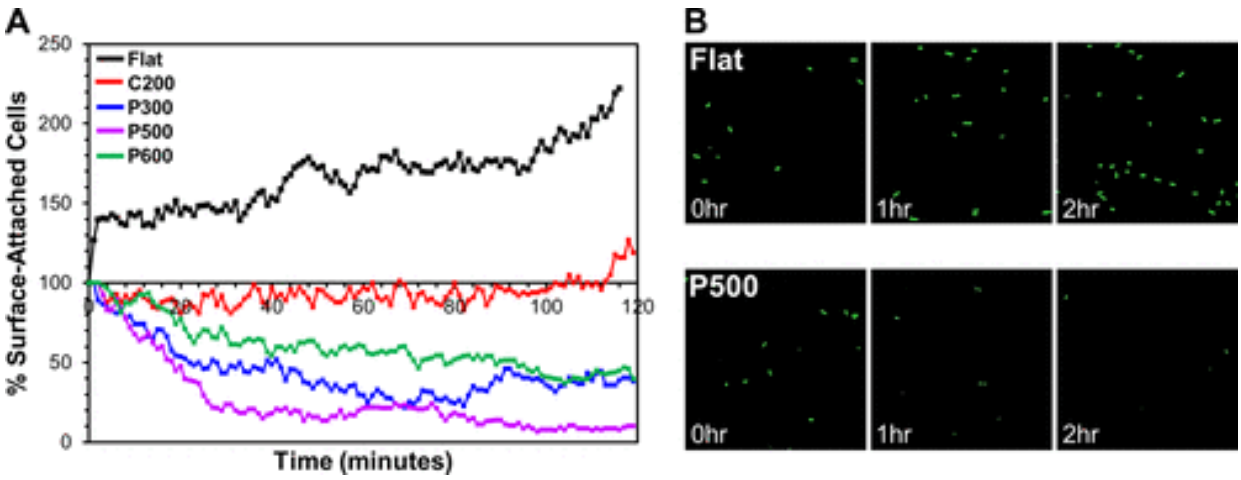

Figure 15. Nanopillared surfaces inhibited the surface attachment of *P. aeruginosa*. Data were collected from 2 h time-lapse videos using an ImageJ TrackMate plugin.[109] (A) Percentage of surface-attached cells on the surfaces was measured in 1 frame each minute for 120 min. A decrease in cell count was observed on the nanopillared surfaces, indicating cell detachment. (B) Images of cells (green) taken at each hour on the flat and P500 surfaces to demonstrate cell division and proliferation on the flat surface and cell detachment on the nanopillared surfaces.

Experimental Methods

Nanopillared Surface Fabrication. Glass coverslips (24 × 60 mm^2) (VWR, Radnor, PA) were treated with 1% aminopropyltriethoxysilane (Sigma-Aldrich, St. Louis, MO) in deionized water (DI) for 20 min to facilitate surface bonding with 120 000 MW poly(methyl methacrylate) (PMMA) (Sigma-Aldrich, Milwaukee, WI) in aqueous solution. PMMA (5% wt) in toluene was spin-coated on the treated glass coverslips at 600 rpm for 45 s. The PMMA-coated coverslips were then annealed on a hot plate at 110 °C for 5 min to evaporate residual solvent. This process was repeated three times to obtain a film thickness of 2 μm. Each PMMA-coated coverslip was then placed in a JenOptik HX03 hot embosser (Jenoptik AG, Jena, Germany) for nanoimprint lithography (NIL). NIL molds previously described[24, 111-113] were centered on top of the PMMA-coated coverslips. A pressure of 2 MPa from the hot embosser top plate was applied to each mold while the PMMA was heated to 70 °C above its glass transition temperature (T_g) from both the top and bottom plates for 20 min. Pressure was maintained while the PMMA was cooled down to and held at room temperatures in the hot embosser for 10 min. Samples were then demolded to reveal nanoimprinted surface structures and sterilized in a fume hood under UV light for 5 min.

Nanopillared Surface Characterization. The flat, C200, P300, P500, and P600 PMMA surfaces were coated with 5 nm of iridium, using an ACE600 sputter coater (Leica Microsystems, Buffalo Grove, IL). The surfaces and their nanostructures were then characterized using a FEI Magellan 400 XHR Scanning Electron Microscope (FEI Company, Hillsboro, OR) at a 45° tilt angle with an acceleration voltage of 3 kV. Contact angle measurements were taken using a OneAttention Theta Optical Tensiometer.

Flow Cell Fabrication. The flow cell channels of 1 mm wide and 25 mm long were cut out from a 100 μm-thick double-sided tape (3 M, Maplewood, MN). The tape with the cut channel was transferred and centered on each PMMA-coated coverslip with either flat or nanopillared surfaces, thus exposing the nanopillars. Blocks of cured poly(dimethylsiloxane) (PDMS) made from a Sylgard 184 silicone elastomer kit (1:10 cross-linker/elastomer base) (Dow Corning, Midland, MI) were cut 50 mm long, 15 mm wide, and 5 mm thick. Inlet and outlet holes, 1 mm in diameter, were precut on the PDMS blocks using a biopsy hole punch. The silicone blocks were placed directly on top of the adhesive tape channels with the holes aligned above the channel ends to provide a flow cell cap. Uncured PDMS was applied on the edges of the PDMS block and cured in an oven at 65 °C for 30 min to seal the cap to the taped PMMA-coated coverslip.

Bacterial Growth Conditions and Flow Cell Loading. *P. aeruginosa* strain AFS64 (PA14 wild-type expressing GFP)[39] was streaked on Luria-broth/Miller (LB) (BD Biosciences, Franklin Lakes, NJ) Petri dishes and incubated for 16 h at 37 °C. Single colonies were each inoculated in 2 mL of sterilized LB media and placed on a rotating incubator for 8 h at 37 °C. The cultures for each experiment were back-diluted in LB to reach a mid-log optical density of 0.2 at 600 nm (OD_{600}).

A 25 cm-long polyethylene (PE) tubing (0.015 in.) was inserted into the flow channel outlet hole and connected to a Petri dish waste container. Another 25 cm-long PE tubing was inserted into the inlet hole and connected to a 1 mL syringe loaded with distilled deionized water (DDI) water with a 27G hypodermic needle. Distilled deionized water (DDI) water was then pumped at 115 μL/min using a Legato 110 Syringe Pump (Fisher Scientific, Holliston, MA) to flush the flow cells and ensure no leakage. The syringe

was then exchanged with a 1 mL syringe loaded with the bacterial cell culture and pumped at 115 μL/min for 8 min until the syringe was empty. The cell solution was static in the channel for ~30 min to allow seeded cells to adhere to the PMMA-coated coverslips before microscopy analysis.

Bacterial Motility Microscopy. The loaded flow channels were immediately placed on an Eclipse Ti inverted research microscope (Nikon, Melville, NY) with NIS-Elements software and imaged using a 100× oil objective at room temperature. Each PMMA-coated surface was observed in triplicate trials. A 25 cm-long tubing was inserted into the outlet hole and connected to a waste container. A 20 mL syringe loaded with only LB media was placed on a syringe pump and connected to a 25 cm-long PE tubing inserted into the flow channel inlet hole. A flow rate of 115 μL/min was applied to the syringe. Time-lapse movies were acquired by obtaining phase images every minute on the flat and nanopillared surfaces for 2–3 h to observe surface-attached cell motility.

Motility Analysis and Quantification. ImageJ was used to track the motility of the bacterial cells from the time-lapse videos. Data were collected from the time-lapse movies using the ImageJ TrackMate plugin.[109] The collected data including cell positions and velocities were analyzed to generate motility analysis plots via MATLAB. Cells (50) with the longest distance traveled from each surface were included in the cell trajectory analysis and normalized to originate at (0,0) (**Figure 12**). The displacement and velocity of all cells were calculated and averaged to construct the average upstream displacement (**Figure 13A**) and average upstream velocity (**Figure 13B**) plots, respectively. For angular trajectories, orientation angles were calculated with respect to the flow direction (**Figure 14A**). The orientation angles of five cells surface-attached for longer than 1 h were tracked

once per minute and displayed in the angular cell trajectories plot (**Figure 14B**). The absolute best-fit angle from the trajectories of cells with the longest distances traveled was calculated and displayed in the angular trajectory histograms (**Figure 14C**). The number of cells was quantified on each flat and nanopillared surface triplicate every minute to obtain the percentage of remaining surface-attached cells relative to the starting time point.

Conclusions and Future Outlook

In summary, we have demonstrated that reducing PMMA surface contact area inhibits upstream motility and persistent attachment of *P. aeruginosa*, a virulent, biofilm-forming bacterium during fluid flow. We used NIL, a cost-effective and scalable method, to fabricate subcellular nanopillared surfaces with varying nanopillar tip packing fractions. The correlation between the decrease in upstream displacement and velocity with the decreasing PMMA nanopillar tip packing fractions provides a new direction in understanding type IV pili mechanoresponses. Additionally, we observed that cell division and proliferation occurred on the flat surfaces, whereas cell detachment and no proliferation occurred on all nanopillared surfaces. The greatest effect was observed on the P500 surface, which had the least net nanopillar tip surface area and packing fraction. Further studies on the trajectories and angular orientations of *P. aeruginosa* during the fluid flow on the flat, C200, P300, P500, and P600 surfaces demonstrated motility inhibition patterns. We have shown that in the case of *P. aeruginosa* under flow conditions, the nanostructuring targets mechanoresponsive properties of bacterial type IV pili to prevent biofilm formation. We conclude that this effect is due to the reduction in surface contact area. Together, these observations present a working model of nanopillared

surfaces in fluid flow environments that disrupt motility and attachment of persistent type IV pili-possessing bacteria. These surfaces have broad applications in industrially and medically relevant systems such as mechanical ventilators, prosthetic heart valves, and catheters. The work presented here can be used as a stepping stone to investigate type IV pili mechanoresponse and regulation of surface attachment in other bacteria for antivirulent and antibiofilm strategies.

CHAPTER 4. Bioinspired Nanotopography Inhibits Drug Resistant Filamentous Fungal Growth

Abstract

Filamentous fungi are invasive and multidrug resistant pathogens that commonly contaminate biomedical devices and implants. Once spherical fungal spores attach to a surface, they exhibit germ tube development, hyphal growth, and robust biofilm formation. Nanotopography found on plants, reptiles, and insect wings possess bactericidal properties during prokaryotic cell adhesion. Here, we demonstrate the application of biomimetic nanopillars that inhibit eukaryotic filamentous fungal growth and possess fungicidal properties. Furthermore, many spores on the nanopillars appeared deflated, while those on the flat surfaces remained spherical and intact. These antifungal phenomena provide promising applications in antifouling biointerfaces for biomedical devices and implants.

Introduction

The kingdom Fungi are of vital ecological, agricultural, and biotechnological importance estimated to have appeared on Earth some 125 million years ago. Fungi have evolved into some 5 million species, approximately 300 of which are known pathogens.[114] Globally, 1.7 billion people suffer from superficial fungal infections,[115] while 1.5 million patient lives are taken from invasive fungal infection as mortality rates exceed 50–90% annually.[116] Fungi kill more humans than malaria and tuberculosis combined worldwide because of their virulence in individuals suffering from immunodeficiencies, HIV, cancer therapies, and immunosuppressive agents in medical treatments.[117-119]

Filamentous fungi, such as *Aspergillus fumigatus* and *Fusarium oxysporum*, produce airborne spores common in the environment,[116] which often sense and adhere to surfaces through membrane bound proteins, ion channels,[119] and fibers.[120] Surface adhesion then initiates the delivery of secretory vesicles to begin biosynthesis of germ tube and hyphal growth proteins.[120] Continuous hyphal extension and cyclic spore secretion results from localized protein clusters in their plasma membrane.[121] During hyphal development, in which pathogenic fungi transition from benign to infection form, filamentous fungi communicate through quorum sensing and secrete extracellular polymeric substance (EPS) for intercellular communication[122] and as communal protection against the environment and pathogenesis.[123] The robust biofilm often leads to threatening conditions in industrial fuel tanks,[124] transplanted organs,[125] and medical devices, such as prosthetic heart valves,[6] joint replacements,[7] contact lenses,[4] and catheters.[9]

Antifungal drugs, such as azoles, polyenes, and fluoropyrimidines, work toward inhibiting fungal cell wall organization and metabolism.[114,117,126] The rigid stress-bearing

cell wall of filamentous fungi consists of 10–20% chitin, 50–60% glucans, and 20–30% glycoproteins[127] and is able to withstand turgor pressure.[128] The walls contain mechanosensitive proteins linked to the skeletal network, which is primarily responsible for maintaining the cell shape, morphogenesis, and osmotic balance.[120,127] The development of antifungal drugs, compared to antibiotics, has been limited due to the challenge of targeting fungi without toxicity to human hosts cells, both eukaryotic sister classes in the tree of life.[129] Filamentous fungi have also gained the mutative ability to alter their gene expression individually and in biofilms to resist common antifungals that are overused in agricultural protection and clinical settings globally.[126] Mechanisms of antifungal resistance include increasing outward efflux of chemical agents, altering agent targeting enzymes, and modifying cellular metabolism.[117] The rise of antimicrobial resistance, including in fungi, bacteria, parasites, and viruses, has led to 1.7 million annual cases of hospital acquired infections, 99 000 deaths,[2] and $16.6 billion spent in healthcare costs in the US alone.[3] There is an urgent need to develop antifungal solutions without the use of chemical agents that may lead to evolved resistance.

Previous work has demonstrated the embedment of biocidal polymers or nanoparticle drugs on surfaces, yet these techniques are not effective for prolonged periods[130,131] and may contribute to the emergence of antimicrobial resistance. The use of biomimetic nanostructured surfaces inspired by the lotus leaf (*Nelumbo nucifera*),[17] gecko foot (*Gekkonidae*),[19] and cicada wing (*Psaltoda claripennis*),[24] nanotopography have shown promise as antibacterial[26] surfaces. Such surfaces have shown adhesion dependent rupture of both bacteria and *Saccharomyces cerevisiae* yeast cells exhibiting comparable size scales to bacteria,[132] yet have not been explored with much larger, robust, and drug resistant

filamentous fungi. Here, we investigate both the antifungal and fungicidal properties of biomimetic, polymeric, nanopillared surfaces inspired by the cicada wing with infection forming filamentous fungi, *A. fumigatus* and *F. oxysporum.* We demonstrate that the nanopillared surfaces fabricated through nanoimprint lithography (NIL) prevent infectious filamentation of surface-attached fungi spores showing promise in antifouling and antibiofilm applications.

Results and Discussion

We began our study by fabricating flat and nanopillared surfaces from poly(methyl methacrylate) (PMMA), an FDA approved polymer commonly used for medical devices. Nanoimprint lithography (NIL), a low-cost and scalable imprinting technique,[25] was employed to fabricate surfaces of biomimetic nanopillars inspired by antibacterial cicada wings using imprinting molds previously described.[24] We fabricated PMMA surfaces with the following notations: flat, C200, P300, and P500 (**Figure 16**). The lettering in the notations represents the imprinting mold originating from either a cicada wing replica or pillared commercial mold replica. The numeric in the notations represents the approximate center-to-center pillar distances in nanometers (**Table 2**).

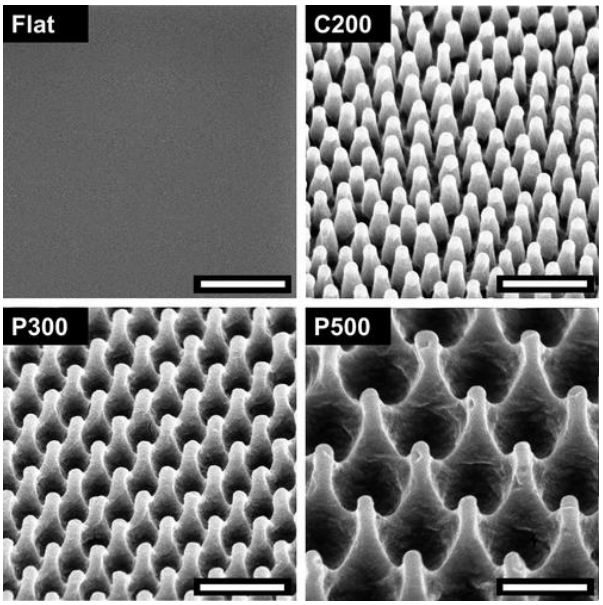

Figure 16. Scanning electron micrographs (SEM) of flat and nanopillared PMMA surfaces taken with 3 kV at a 45° tilt. Flat surfaces were fabricated through spin coating. C200, P300, and P500 nanopillared surfaces were fabricated through spin coating followed by nanoimprint nanoimprint lithography (NIL). The lettering in the nomenclature represents the negative imprinting mold originating from either a cicada wing or pillared master mold. The numeric in the nomenclature represents the center-to-center nanometer pillar periodicities. Scale bars represent 500 nm.

We next inoculated 1×10^5 total spores of filamentous fungi, *A. fumigatus* and *F. oxysporum,* onto triplicate surfaces of each pattern in polystyrene wells and incubated them at 37 °C and 34 °C, respectively. Spores were swollen in Sabouraud Dextrose (SD) broth for 6 h and then inoculated on the surfaces to compare the germ tube development, hyphal growth, and biofilm formation between the flat and nanopillared surfaces. The surfaces were then mounted on an inverted microscope. Phase images were taken every 8 h to monitor surface-attached cell growth (**Figures 17A and 17B**). On the flat surfaces, spores germinated to develop germ tubes, followed by hyphae, and eventually biofilm. By contrast, germ tubes were inhibited on the nanopillared surfaces and no hyphae or biofilm formed. The greatest inhibition of growth was observed on the P500 surfaces, which has the largest nanopillar periodicity among the nanopillared surfaces studied in this work (**Figure 18A and B)**

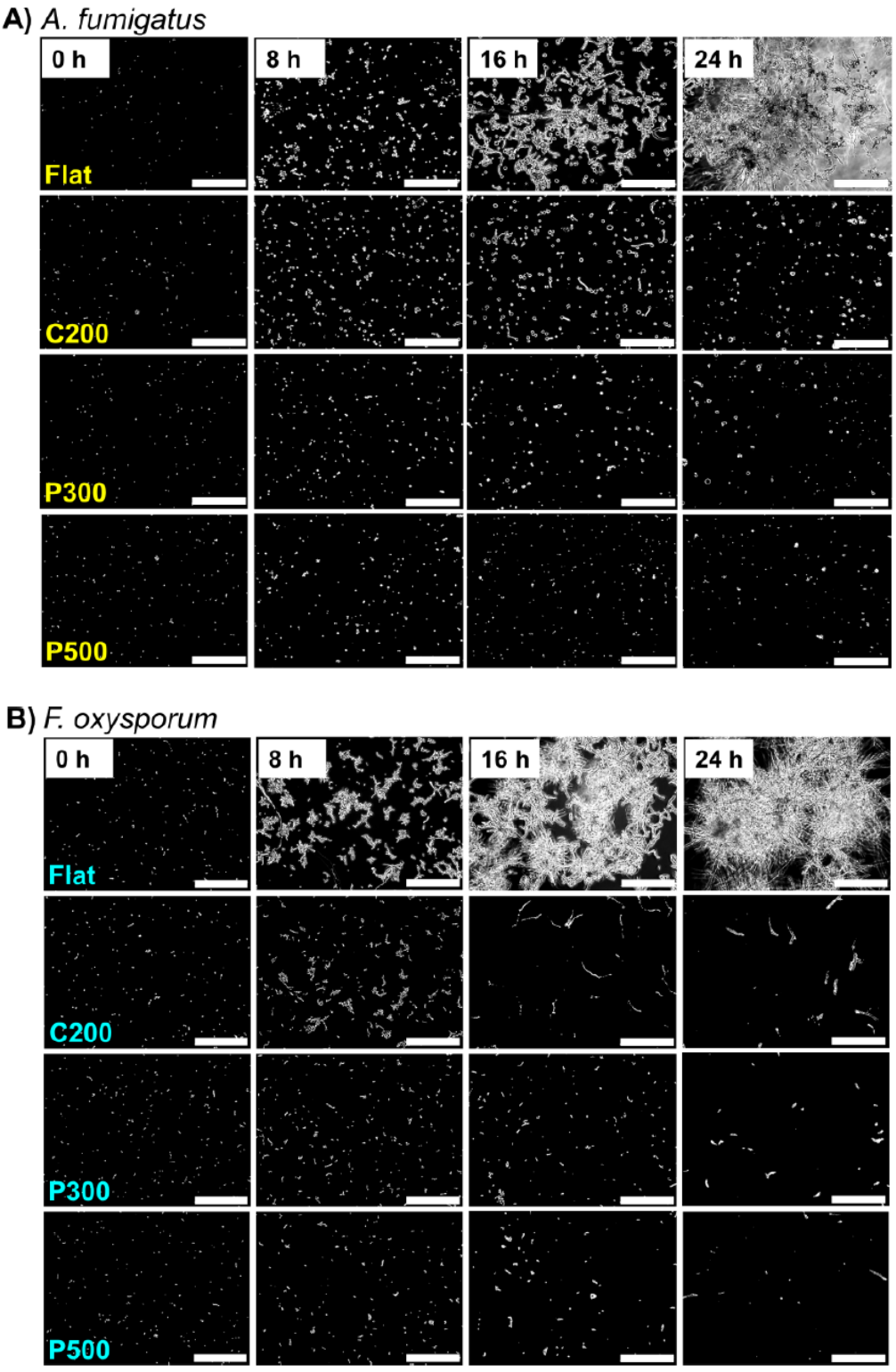

Figure 17. Nanopillared surfaces demonstrated antifungal properties of (A) *A. fumigatus* grown at 37 °C and (B) *F. oxysporum* grown at 34 °C. Cells were swollen for 6 h in SD broth and then inoculated in triplicate wells with flat, C200, P300, and P500 bottom surfaces. Images were taken every 8 h to observe fungal germ tube development, hyphal growth, and biofilm formation on the flat surfaces. Growth inhibition was observed on the nanopillared surfaces with eventual cell detachment. Scale bars represent 200 μm.

Among the nanopillared surfaces, the antifungal effect was, in order, flat < C200 < P300 < P500 (**Figure 18**). These results are different from previous studies of prokaryotic Gram-negative bacteria growth inhibition on nanopillared surfaces, where the smallest pillar periodicities studied were most effective.[24] These contrasts may be related to the size scale differences in cell wall architecture and membrane mechanosensing. On these nanopillared surfaces, germ tube development was disrupted and spores began to detach after 16 h for *A. fumigatus* and 8 h for *F. oxysporum.* After 24 h of surface attachment, cells from each surface were plated on SD agar to evaluate if the cells were alive or dead after surface attachment on the nanopillars. Colony forming units (CFU) formed on the agar were counted, and we found significantly fewer CFUs from the cells taken from the nanopillared surfaces compared with the flat surfaces (**Figure 18C, 18D, and 18E**). *F. oxysporum* CFUs decreased from C200 to P300 to P500 surfaces, demonstrating that these nanopillared surfaces have not only antifungal but also fungicidal effects (**Figure 18C, 18D, and 18E**). The higher CFU count from cells taken from flat surfaces demonstrate that initial surface-attached spores became filamentous and persisted with their cyclic hyphal spore secretion.

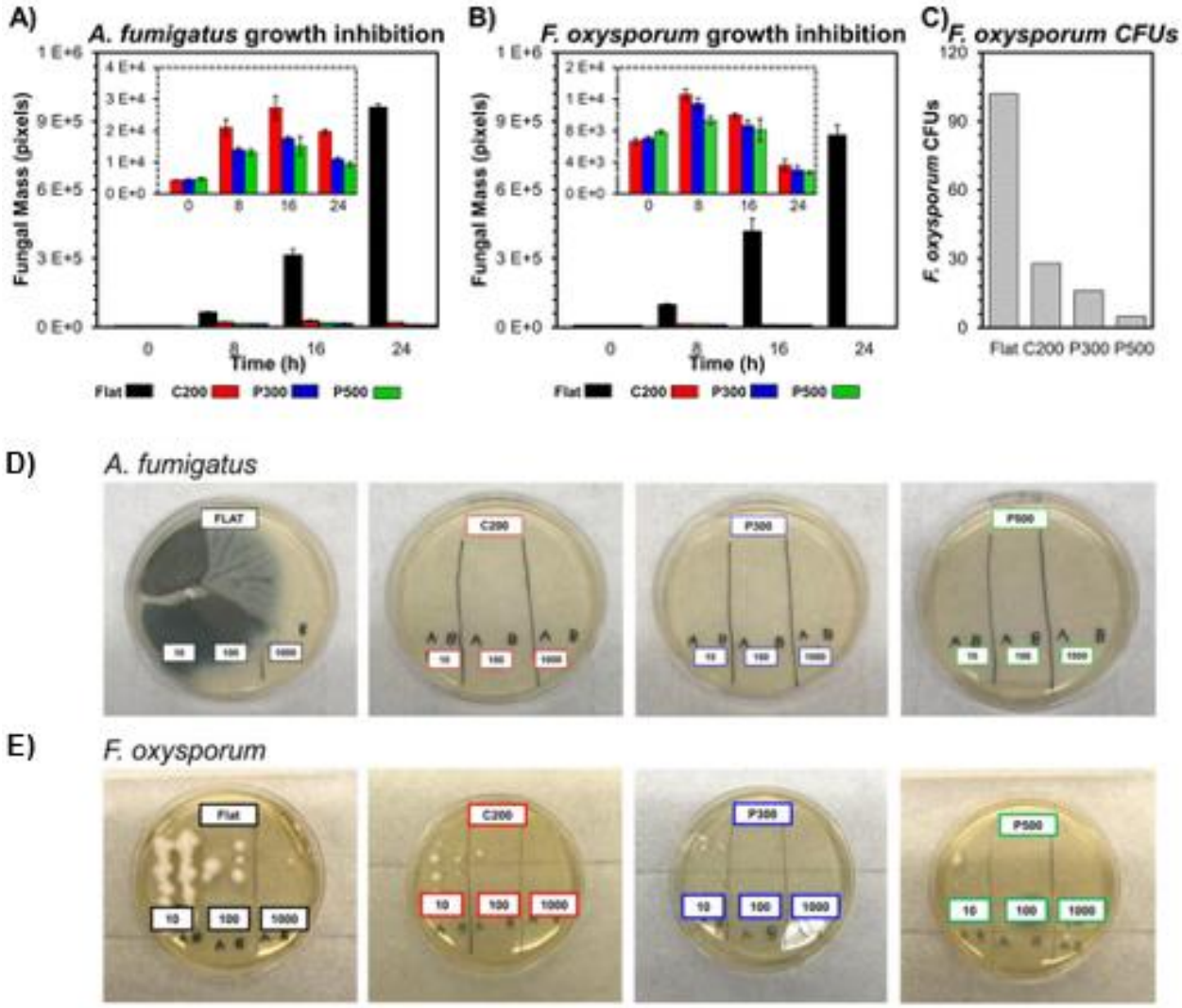

Figure 18. Nanopillared surfaces demonstrated antifungal and fungicidal properties. (A) *A. fumigatus* growth was inhibited on the nanopillared surfaces with cell detachment observed after 16 h (inset). (B) *F. oxysporum* growth was inhibited on the nanopillared surfaces with cell detachment observed after 8 h (inset). (C) *F. oxysporum* planktonic cells were taken from each well after 24 h and seeded on SD agar plates to grow for 48 h at 34 °C. The nanopillared surfaces showed fungicidal properties as less CFUs formed. (D) *A. fumigatus* and (E) *F. oxysporum* planktonic cells taken from flat and nanopatterned surfaces after 24 hours to grown on SD agar incubated at 37C and 34 C, respectively, to assess fungal cell death.

We then analyzed the cell membrane-to-nanopillar interaction with scanning electron microscopy (SEM) (**Figure 19**). Prior to imaging, spores were fixed with 4% paraformaldehyde and dehydrated with serial ethanol dilutions. Surfaces were then sputter coated with 5 nm of iridium to form a conductive layer suitable for SEM *A. fumigatus* and *F. oxysporum* spores exhibited spherical configurations on the flat surfaces

along with areas of filamentous biofilm formation, while spores on the nanopillared surfaces were often found deflated with limited germ tube development. *A. fumigatus* spores on the nanopillared surfaces were either found to be spherical, deflated in the center of the spore, deflated on half of the spore, or completely deflated after 24 h (**Figure 19C**). While the fixing and dehydration of cells during SEM preparation resulted in cell wall shriveling on all surfaces, full deflation was primarily observed on the nanopillared surfaces.

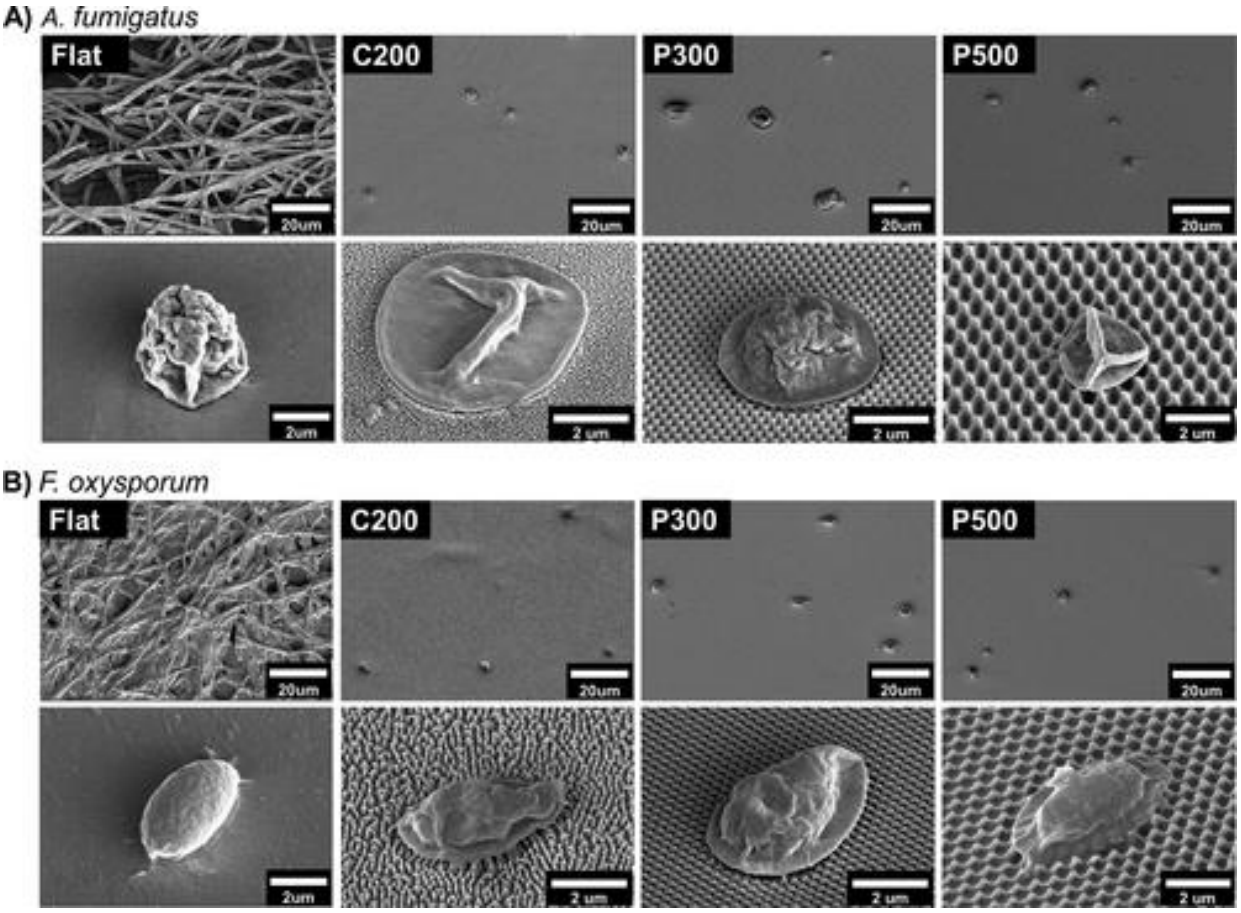

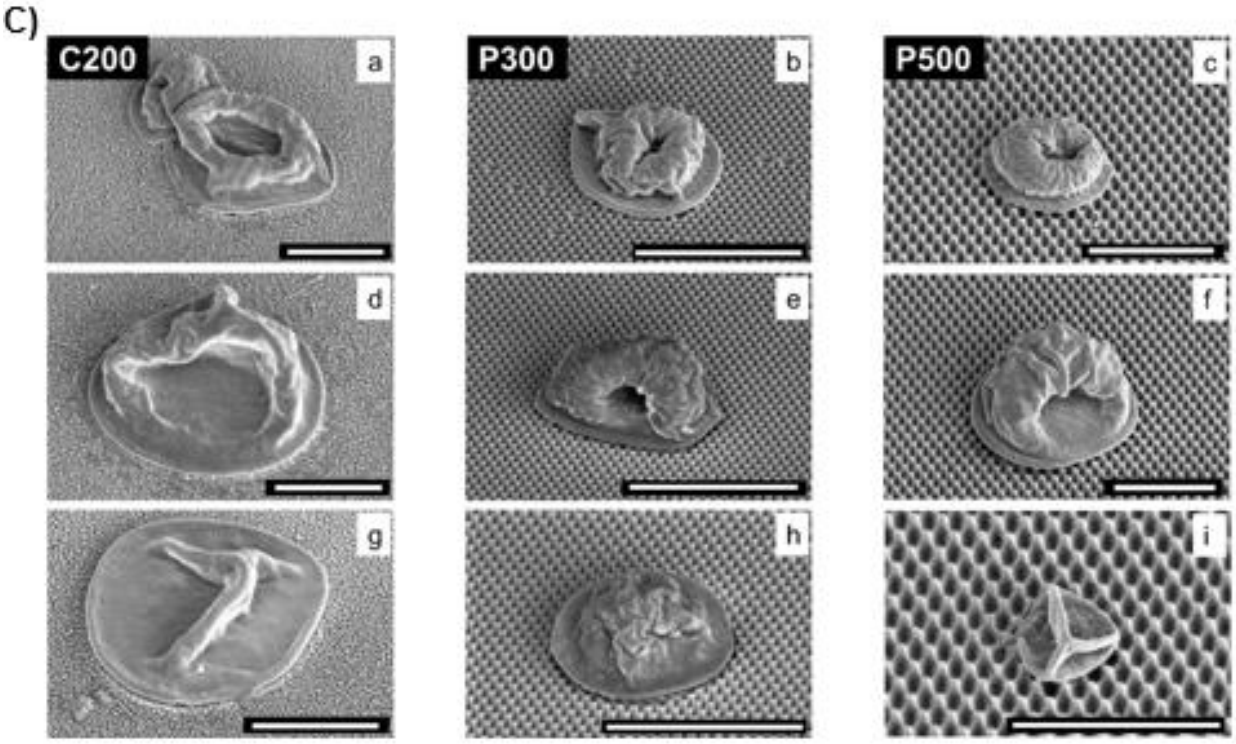

Figure 19. Scanning electron micrographs (SEMs) of fungal growth on flat and nanotopography. Biofilm formation of (A) *A. fumigatus* and (B) *F. oxysporum* was present on the flat surfaces, along with intact hyphal secreted spores, while levels of deflated spores were present on the nanopillared surfaces. (C) Scanning electron micrographs of A. fumigatus on C200, P300, and P500 surfaces. (a - c) Cell were commonly found deflated in the cell body center. (d - f) Cells were commonly found partially deflated in a crescent cell body shape. (g - i) Cells were commonly found fully deflated. Scale bars represent 5um.

We further investigated the interaction between the damaged and apparently deflated *A. fumigatus* germ tube cell membrane and the P300 nanopillared surface (**Figure 20**). The presence of adhesion substance on both the membrane and nanopillars indicates that adhesion of the cell to the surface had occurred before hyphal growth inhibition. The fungal cell possesses many membrane-bound mechanosensitive proteins responsible for maintaining cell growth and metabolism.[120,127] Further investigations into the biophysical phenomena within the spores and germ tubes during growth inhibition on nanopillars would shed light on the antifungal surface mechanism.

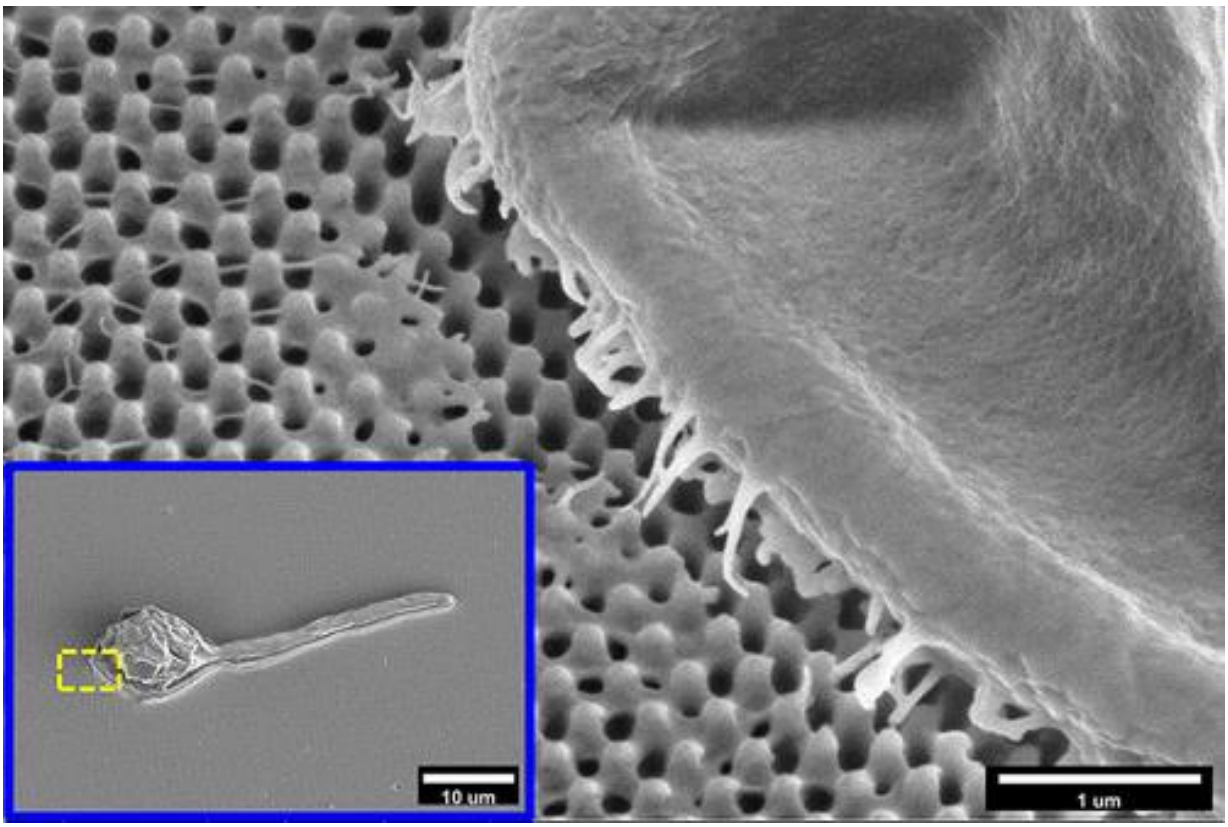

Figure 20. Scanning electron micrographs (SEMs) of surface-attached *A. fumigatus* on nanotopography. *A. fumigatus* cells were surface-attached and able to sense the nanopillars before growth inhibition as shown with the presence of adhesion substance.

Experimental Methods

Nanopillared Surface Fabrication. Glass coverslips (24 × 60 mm^2) (VWR, Radnor, PA) were treated with 1% aminopropyltriethoxysilane (Sigma-Aldrich, St. Louis, MO) in deionized water (DI) for 20 min to facilitate surface bonding with 120 000 MW poly(methyl methacrylate) (PMMA) (Sigma-Aldrich, Milwaukee, WI) in aqueous solution. PMMA (5% wt) in toluene was spin-coated on the treated glass coverslips at 600 rpm for 45 s. The PMMA-coated coverslips were then annealed on a hot plate at 110 °C for 5 min to evaporate residual solvent. This process was repeated three times to obtain a film

thickness of 2 μm. Each PMMA-coated coverslip was then placed in a JenOptik HX03 hot embosser (Jenoptik AG, Jena, Germany) for nanoimprint lithography (NIL). NIL molds previously described[24,111-113] were centered on top of the PMMA-coated coverslips. A pressure of 2 MPa from the hot embosser top plate was applied to each mold while the PMMA was heated to 70 °C above its glass transition temperature (T_g) from both the top and bottom plates for 20 min. Pressure was maintained while the PMMA was cooled down to and held at room temperatures in the hot embosser for 10 min. Samples were then demolded to reveal nanoimprinted surface structures and sterilized in a fume hood under UV light for 5 min.

Nanopillared Surface Characterization. The flat, C200, P300, P500, and P600 PMMA surfaces were coated with 5 nm of iridium, using an ACE600 sputter coater (Leica Microsystems, Buffalo Grove, IL). The surfaces and their nanostructures were then characterized using a FEI Magellan 400 XHR Scanning Electron Microscope (FEI Company, Hillsboro, OR) at a 45° tilt angle with an acceleration voltage of 3 kV.

Fungal Growth Conditions. *A. fumigatus* and *F. oxysporum* cells were taken from frozen stocks and streaked on Sabouraud Dextrose (SD) agar plates. *A. fumigatus* cell were incubated at 37C for seven days, while *F. oxysporum* cells were incubated at 34C for four days. The cells were then washed with SD broth and filtered into 50mL centrifuge tubes to isolate the spores from the germ tubes and hyphae. The spores were next swollen for six hours in SD broth and back diluted to a 1 x 10^5 spore count when inoculated into the triplicate PMMA surfaces of each flat or nanopillared pattern in polystyrene wells.

Fungal Growth Microscopy. *A. fumigatus* and *F. oxysporum* spores on each surface were mounted on a BioTek Cytation5 inverted microscope. Phase images were taken every

eight hours between *A. fumigatus* incubations at 37C and *F. oxysporum* incubations at 34C to observe their germ tube development, hyphal growth, and biofilm formation of surface-attached cells. ImageJ was used to quantify fungal mass in pixel area on each surface.

Fungal Scanning Electron Microscopy. Each surface was prepared for scanning electron microscopy after each 24 hours of surface-attached cell growth. The SD broth in each well was slowly aspirated out and replaced with 2mL of 4% paraformaldehyde (PFA) for 20 minutes to allow fixation of surface-attached cells. Then, the PFA was slowly aspirated out and replaced with 50% ethanol in DI water for 15 minutes. A series of 15-minute serial dilutions followed with 70%, 80%, 90%, 95%, and 100% ethanol in DI water for each surface for completed dehydration of the surface-attached cells. Cells were left in a fume hood overnight to fully dry before being coated with 5nm of iridium, using an ACE600 sputter coater (Leica Microsystems, Buffalo Grove, IL) to provide a conductive coating suitable for scanning electron microscopy imaging. The surface-attached cells on each surface were then characterized using a FEI Magellan 400 XHR Scanning Electron Microscope (FEI Company, Hillsboro, OR) at a 45^{o} tilt angle and an acceleration voltage of 3 kV.

Fungal CFU Analysis. Cells from each surface were seeded onto SD agar plates after each 24 hours of surface-attached cell growth to evaluate if the cells were alive or dead. *A. fumigatus* cells were grown for 72 hours at 37C and *F. oxysporum* cells were grown for 48 hours at 34C. Images were then taken to observe and count each colony formed form each surface at 1:10, 1:100, and 1:1000 dilutions.

Conclusions and Future Outlook

In conclusion, we demonstrated the use of scalable nanopillared surface fabrication via NIL to inhibit the growth of invasive, drug-resistant, biofilm-forming, filamentous fungi *A. fumigatus* and *F. oxysporum*. Notably, filamentous fungal spores detached from the nanopillars after 16 h for *A. fumigatus* and 8 h for *F. oxysporum.* The P500 surfaces, which possessed nanopillars with the greatest periodicity, exhibited the largest antifungal and fungicidal effects. High spatiotemporal resolution microscopy of the filamentous fungal membrane-bound mechanosensitive protein contact with the nanopillared surfaces would provide insight on the adhesive effects of the antifungal and fungicidal properties. Additionally, further investigation into the membrane-bound mechanosensitive proteins that control cell growth and metabolism would shed light on the biophysical mechanism. Understanding these biological phenomena could serve as a gateway for developing other drug-free, nanopillared, antimicrobial surfaces that are suitable for industrial, commercial, and healthcare applications.

CHAPTER 5. Conclusions and Future Outlook on Biophysical Mechanisms

In this work, we demonstrated that bioinspired nanotopography inhibits the surface attachment of several microbial effects that may shed light on new platforms to study microbial mechanobiology. We found that virulence of surface-attached *P. aeruginosa* in an amoeba host killing assay was hindered on the C200, P300, and P500 surfaces, yet many questions remain such as (1) What role do surface-attachment pili play? (2) What role does the pilY1 protein play? and (3) Is quorum sensing inhibited? The experiments conducted involved PA14 along with knockout mutants PilTU, FlgK, and PilTU-FlgK lacking specific motility and surface sensing appendages or both. Further studies should involve mutant knockouts lacking other pili involved in surface sensing along and the PilY1 protein. Measurements of secondary metabolites secreted during virulence activity such as pyocyanin could be measured as an additional assay. Such phenazines cause ciliary dysfunction in the respiratory tract and exert oxidative effects and inflammation to damage host cells.[72] Measurements of quorum sensing signaling molecules should also be conducted to verify if quorum sensing, required for biofilm formation, is hindered on virulence inhibiting nanotopography. Such information would provide further knowledge in microbial chemical signaling and communication influenced by surface topography. Quantitative studies would also be beneficial to track not only cellular growth on nanotopography but identifying the which specific point in the cell cycle are hindered.

Additionally, we demonstrated that bioinspired nanotopography disrupted *P. aeruginosa* mechanoresponsive upstream motility using cell tracking from microscopy analysis of cells in fabricated flow cells with nanopillared bottom surfaces. Several

questions concerning the mechanoresponsive cellular appendage remain such as (1) What role do surface-attachment pili play? (2) What role do the molecular motors play? And (3) Can we image the pili and nanopillar interaction? In 2016, Chang, *et al.*[133] demonstrated the use of cryo-electron tomography to image and reconstruct the architecture of the bacterium *Myxococcus xanthus* type IV pili and its molecular motors at play. Further studies could image the interaction of the type IV pili in fluid flow systems with tips of nanotopography and possibly the molecular motor activity. The use of cryo-electron tomography may also reveal cell wall activity when adhered to nanotopography as cell wall synthesis is involved in recovery of plastic deformation due to bending forces.[134,135]

Lastly, we demonstrated that bioinspired nanotopography inhibited *A. fumigatus* and *F. oxysporum* filamentous fungal growth, which presents a new antimicrobial system. This discovery opens up new scientific questions such as (1) Is fungal virulence inhibited? (2) What role do fungal membrane mechanosensors play? and (3) Do the biophysical mechanisms relate to prokaryotic cells? Since 1997, fungal filamentation has been demonstrated a process enabling surface-attached fungi to switch from benign to infection forming as nonfilamentous *Candida albicans* mutants were avirulent.[136,137] Further studies should develop virulence assays for filamentous fungi *A. fumigatus* and *F. oxysporum* to provide future advancements in antifungal strategies. Both bacteria and fungi possess mechanosensitive membrane bound proteins, ion channels,[119] and fibers[120] responsible for surface sensing and various biochemical processes relevant to cellular survival. The investigation of microbial mechanosensitive channels utilizing mutant knockout strains to analyze the antimicrobial effect on nanotopography opens doors to new scientific

questions in membrane ion channel activity influences by possible tension, [138-142] mechanosensation,[143-147] and communication[148] on nanostructures.

In conclusion, we have demonstrated in this work several methods of inhibiting the formation of infectious biofilms. Future work could include *in vitro* and *in vivo* studies on the antimicrobial effects in comparison and in combination synergistically with antimicrobial drugs. As the bioinspired nanotopography inhibits microbial growth and motility, these effects may combat microbial infections when combined with other methods that are declining in efficacy. Furthermore, these bioinspired nanotopography may provide a new platform to study mechanobiology. Future surfaces could be tailored using the fabrication methods described in Chapter 1 to study the cell-surface interface and biophysical effects in tailored nanofeature surface patterns with varying pillar shapes, geometries, and radii of curvatures. Next steps in studying the biophysical mechanisms of such antimicrobial nanotopographies would be to perform RNA sequences to study which genes in each microbe are being up or down regulated and coordinate such results with biophysical effects[149]. A further study should involve investigating possible mechanobiological resistance mechanisms to nanotopography as it has been shown that *P. aeruginosa* possess multigenerational memory and adaptive adhesion.[150] The applications of bioinspired nanotopography reaches far beyond solutions for antimicrobial surfaces and may provide a convergence of studies in materials science, engineering, and microbiology to explore the newer field of mechanobiology.

REFERENCES

1. Lax, S.; Sangwan, N.; Smith, D.; Larsen, P.; Handley, K. M.; Richardson, M.; Guyton, K.; Krezalek, M.; Shogan, B. D.; Defazio, J.; Flemming, J.; Shaksheer, B.; Weber, S.; Landon, E.; Garcia-Houchins, S.; Siegel, J.; Alverdy, J.; Knight, R.; Stephens, B.; Gilbert, J. A. Bacterial Colonization and Succession in a Newly Opened Hospital. *Science Translational Medicine* **2017**, *9* (391), eaah6500.

2. Klevens, R. M.; Edwards, J. R.; Richards, C. L.; Horan, T. C.; Gaynes, R. P.; Pollock, D. A.; Cardo, D. M. Estimating Health Care-Associated Infections and Deaths in U.S. Hospitals, 2002. *Public Health Reports* **2007**, *122* (2), 160–166.

3. Hassan, M.; Tuckman, H. P.; Patrick, R. H.; Kountz, D. S.; Kohn, J. L. Cost of Hospital-Acquired Infection. *Hospital Topics* **2010**, *88* (3), 82–89.

4. Imamura, Y.; Chandra, J.; Mukherjee, P. K.; Lattif, A. A.; Szczotka-Flynn, L. B.; Pearlman, E.; Lass, J. H.; O'Donnell, K.; Ghannoum, M. A. *Fusarium* and *Candida albicans* Biofilms on Soft Contact Lenses: Model Development, Influence of Lens Type, and Susceptibility to Lens Care Solutions. *Antimicrobial Agents and Chemotherapy* **2008**, *52* (1), 171–182.

5. Domitrovic, T. N.; Hujer, A. M.; Perez, F.; Marshall, S. H.; Hujer, K. M.; Woc-Colburn, L. E.; Parta, M.; Bonomo, R. A. Multidrug Resistant *Pseudomonas aeruginosa* Causing Prosthetic Valve Endocarditis: A Genetic-Based Chronicle of Evolving Antibiotic Resistance. *Open Forum Infect Dis* **2016**, *3* (4), ofw188.

6. Gage, A. A. *Aspergillus* Infection After Cardiac Surgery. *Arch Surg* **1970**, *101* (3), 384.

7. Hwang, B.-H.; Yoon, J.-Y.; Nam, C.-H.; Jung, K.-A.; Lee, S.-C.; Han, C.-D.; Moon, S.-H. Fungal Peri-Prosthetic Joint Infection after Primary Total Knee Replacement. *The Journal of Bone and Joint Surgery. British volume* **2012**, *94-B* (5), 656–659.

8. Stamm, W. E. Catheter-Associated Urinary Tract Infections: Epidemiology, Pathogenesis, and Prevention. *The American Journal of Medicine* **1991**, *91* (3), S65–S71.

9. Pittet, D. Nosocomial Bloodstream Infections: Secular Trends in Rates, Mortality, and Contribution to Total Hospital Deaths. *Arch Intern Med* **1995**, *155* (11), 1177.

10. O'Neill, J. Review in Antimicrobial Resistance: Tackling a Crisis for the Health and Wealth of Nations. *UK Government and Wellcome Trust* **2014**.

11. Mah, T.-F. C.; O'Toole, G. A. Mechanisms of Biofilm Resistance to Antimicrobial Agents. *Trends in Microbiology* **2001**, *9* (1), 34–39.

12. Mah, T.-F.; Pitts, B.; Pellock, B.; Walker, G. C.; Stewart, P. S.; O'Toole, G. A. A Genetic Basis for *Pseudomonas aeruginosa* Biofilm Antibiotic Resistance. *Nature* **2003**, *426*, 306-310.

13. Miller, M. B.; Bassler, B. L. Quorum Sensing in Bacteria. *Annual Review Microbiology* **2001**, 55, 165-199.

14. Hall-Stoodley, L.; Costerton, J. W.; Stoodley, P. Bacterial Biofilms: From the Natural Environment to Infectious Diseases. *Nature Reviews Microbiology* **2004**, *2* (2), 95–108.

15. Blair, J. M. A.; Webber, M. A.; Baylay, A. J.; Ogbolu, D. O.; Piddock, L. J. V. Molecular Mechanisms of Antibiotic Resistance. *Nature Review Microbiology* **2015**, *13* (1), 42–51.

16. Chung, K. K.; Schumacher, J. F.; Sampson, E. M.; Burne, R. A.; Antonelli, P. J.; Brennan, A. B. Impact of engineered surface microtopography on biofilm formation of *Staphylococcus aureus*. *Biointerphases* **2007**, 2, 89–94.

17. Barthlott, W.; Neinhuis, C. Purity of the Sacred Lotus, or Escape from Contamination in Biological Surfaces. *Planta* **1997**, *202* (1), 1–8.

18. Bandara, C. D.; Singh, S.; Afara, I. O.; Wolff, A.; Tesfamichael, T.; Ostrikov, K.; Oloyede, A. Bactericidal Effects of Natural Nanotopography of Dragonfly Wing on *Escherichia coli*. *ACS Applied Materials and Interfaces* **2017**, 9(8), 6746-6760.

19. Watson, G. S.; Green, D. W.; Schwarzkopf, L.; Li, X.; Cribb, B. W.; Myhra, S.; Watson, J. A. A Gecko Skin Micro/Nano Structure – A Low Adhesion, Superhydrophobic, Anti-Wetting, Self-Cleaning, Biocompatible, Antibacterial Surface. *Acta Biomaterialia* **2015**, *21*, 109–122.

20. D'Alba, L.; Jones, D. N.; Badawy, H. T.; Eliason, C. M.; Shawkey, M. D. Antimicrobial Properties of a Nanostructured Eggshell from a Compost-Nesting Bird. *Journal of Experimental Biology* **2014**, *217* (7), 1116–1121.

21. Hanson, L.; Zhao, W.; Lou, H-Y.; Lin, Z. C.; Lee, S. W.; Chowdary, P.; Cui, Y.; Cui, B. Vertical Nanopillars for *in situ* Probing of Nuclear Mechanics in Adherent Cells. *Nature Nanotechnology* **2015**, 10, 554–562.

22. Cao, Y.; Hjort, M.; Chen, H.; Birey, F.; Leal-Ortiz, S. A.; Han, C. M.; Santiago, J. G.; Pasca, S. P.; Wu, J. C.; Melosh, N. A. Nondestructive Nanostraw Intracellular Sampling for Longitudinal Cell Monitoring. *Proceedings of the National Academy of Sciences* **2017**, 114(10), 1866-1874.

23. Tripathy, A.; Sen, P.; Su, B.; Briscoe, W. H. Natural and Bioinspired Nanostructured Bactericidal Surfaces. *Advances in Colloid and Interface Science* **2017**, *248*, 85–104.

24. Dickson, M. N.; Liang, E. I.; Rodriguez, L. A.; Vollereaux, N.; Yee, A. F. Nanopatterned Polymer Surfaces with Bactericidal Properties. *Biointerphases* **2015**, *10* (2), 021010.

25. Tan, L.; Kong, Y. P.; Bao, L.-R.; Huang, X. D.; Guo, L. J.; Pang, S. W.; Yee, A. F. Imprinting Polymer Film on Patterned Substrates. *J. Vac. Sci. Technol., B: Microelectron. Nanometer Struct.–Process., Meas., Phenom.* **2003**, 21, 2742.

26. Rosenzweig, R.; Perinbam, K.; Ly, V. K.; Ahrar, S.; Siryaporn, A.; Yee, A. F. Nanopillared Surfaces Disrupt *Pseudomonas aeruginosa* Mechanoresponsive Upstream Motility. *ACS Applied Materials and Interfaces* **2019**, *11* (11), 10532–10539.

27. Rosenzweig, R.; Marshall, M.; Parivar, A.; Ly, V. K.; Pearlman, E.; Yee, A. F. Biomimetic Nanopillared Surfaces Inhibit Drug Resistant Filamentous Fungal Growth. *ACS Applied Bio Materials* **2019**, *2*, 3159-3163.

28. Ivanova, E. P.; Hasan, J.; Webb, H. K.; Truong, V. K.; Watson, G. S.; Watson, J. A.; Baulin, V. A.; Pogodin, S.; Wang, J. Y.; Tobin, M. J.; Lobbe, C.; Crawford, R. J. Natural Bactericidal Surfaces: Mechanical Rupture of Pseudomonas aeruginosa Cells by Cicada Wings. *Small* **2012**, 8, 2489–2494.

29. Pogodin, S.; Hasan, J.; Baulin, V. A.; Webb, H. K.; Truong, V. K.; Phong Nguyen, T. H.; Boshkovikj, V.; Fluke, C. J.; Watson, G. S.; Watson, J. A.; Crawford, R. J.; Ivanova, E. P. Biophysical Model of Bacterial Cell Interactions with Nanopatterned Cicada Wing Surfaces. *Biophysical Journal* **2013**, *104* (4), 835–840.

30. Diu, T.; Faruqui, N.; Sjöström, T.; Lamarre, B.; Jenkinson, H. F.; Su, B.; Ryadnov, M. G. Cicada-Inspired Cell-Instructive Nanopatterned Arrays. *Scientific Reports* **2015**, *4* (1), 7122.

31. Persat, A. Bacterial Mechanotransduction. *Current Opinion in Microbiology* **2017**, *36*, 1–6.

32. Persat, A.; Nadell, C. D.; Kim, M. K.; Ingremeau, F.; Siryaporn, A.; Drescher, K.; Wingreen, N. S.; Bassler, B. L.; Gitai, Z.; Stone, H. A. The Mechanical World of Bacteria. *Cell* **2015**, *161* (5), 988–997.

33. O'Toole, G. A.; Wong, G. C. Sensational Biofilms: Surface Sensing in Bacteria. *Current Opinion in Microbiology* **2016**, *30*, 139–146.

34. Gordon, V. D.; Wang, L. Bacterial Mechanosensing: The Force Will Be with You, Always. *Journal of Cell Science* **2019**, *132* (7), jcs227694.

35. O'Toole, G. A.; Kolter, R. Flagellar and Twitching Motility Are Necessary for *Pseudomonas aeruginosa* Biofilm Development. *Molecular Microbiology* **1998**, *30* (2), 295–304.

36. Hughes, K. T.; Berg, H. C. The Bacterium Has Landed. *Science* **2017**, *358* (6362), 446–447.

37. Lele, P. P.; Hosu, B. G.; Berg, H. C. Dynamics of Mechanosensing in the Bacterial Flagellar Motor. *Proceedings of the National Academy of Sciences* **2013**, *110* (29), 11839–11844.

38. Liang, E. I.; Mah, E. J.; Yee, A. F.; Digman, M. A. Correlation of Focal Adhesion Assembly and Disassembly with Cell Migration on Nanotopography. *Integrative Biology* **2017**, 9(2), 145-155.

39. Siryaporn, A.; Kuchma, S. L.; O'Toole, G. A.; Gitai, Z. Surface Attachment Induces *Pseudomonas aeruginosa* Virulence. *Proceedings of the National Academy of Sciences* **2014**, *111* (47), 16860–16865.

40. Kuchma, S. L.; Ballok, A. E.; Merritt, J. H.; Hammond, J. H.; Lu, W.; Rabinowitz, J. D.; O'Toole, G. A. Cyclic-Di-GMP-Mediated Repression of Swarming Motility by *Pseudomonas aeruginosa*: The PilY1 Gene and Its Impact on Surface-Associated Behaviors. *Journal of Bacteriology* **2010**, *192* (12), 2950–2964.

41. Luo, Y.; Zhao, K.; Baker, A. E.; Kuchma, S. L.; Coggan, K. A.; Wolfgang, M. C.; Wong, G. C. L.; O'Toole, G. A. A Hierarchical Cascade of Second Messengers Regulates *Pseudomonas aeruginosa* Surface Behaviors. *mBio* **2015**, *6* (1), e02456-14.

42. Heiniger, R. W.; Winther-Larsen, H. C.; Pickles, R. J.; Koomey, M.; Wolfgang, M. C. Infection of Human Mucosal Tissue by *Pseudomonas aeruginosa* Requires Sequential and Mutually Dependent Virulence Factors and a Novel Pilus-Associated Adhesin: Factors Involved in *P. aeruginosa* Tissue Infection. *Cellular Microbiology* **2010**, *12* (8), 1158–1173.

43. Armbruster, C. R.; Lee, C. K.; Parker-Gilham, J.; de Anda, J.; Xia, A.; Zhao, K.; Murakami, K.; Tseng, B. S.; Hoffman, L. R.; Jin, F.; Harwood, C. S.; Wong, G.C.L.; Parsek, M. R. Heterogeneity in Surface Sensing Suggests a Division of Labor in *Pseudomonas aeruginosa* Populations. *eLife* **2019**, *8*, e45084.

44. Laventie, B.-J.; Sangermani, M.; Estermann, F.; Manfredi, P.; Planes, R.; Hug, I.; Jaeger, T.; Meunier, E.; Broz, P.; Jenal, U. A Surface-Induced Asymmetric Program Promotes Tissue Colonization by *Pseudomonas aeruginosa*. *Cell Host & Microbe* **2019**, *25* (1), 140-152.e6.

45. Perinbam, K.; Siryaporn, A. A Rapid Image-Based Bacterial Virulence Assay Using Amoeba. *JoVE* **2018**, No. 136, 57844.

46. Cosson, P.; Zulianello, L.; Join-Lambert, O.; Faurisson, F.; Gebbie, L.; Benghezal, M.; van Delden, C.; Curty, L. K.; Kohler, T. *Pseudomonas aeruginosa* Virulence Analyzed in a Dictyostelium Discoideum Host System. *Journal of Bacteriology* **2002**, *184* (11), 3027–3033.

47. Pukatzki, S.; Kessin, R. H.; Mekalanos, J. J. The Human Pathogen *Pseudomonas aeruginosa* Utilizes Conserved Virulence Pathways to Infect the Social Amoeba

Dictyostelium Discoideum. *Proceedings of the National Academy of Sciences* **2002**, *99* (5), 3159–3164.

48. Alibaud, L.; Köhler, T.; Coudray, A.; Prigent-Combaret, C.; Bergeret, E.; Perrin, J.; Benghezal, M.; Reimmann, C.; Gauthier, Y.; van Delden, C.; Attree, I.; Fauvarque, M-O.; Cosson, P. *Pseudomonas aeruginosa* Virulence Genes Identified in a Dictyostelium Host Model. *Cellular Microbiology* **2008**, *10* (3), 729–740.

49. Bartell, J. A.; Blazier, A. S.; Yen, P.; Thogersen, J. C.; Jelsbak, L.; Goldberg, J. B.; Papin, J. A. Reconstruction of the Metabolic Network of *Pseudomonas aeruginosa* to Interrogate Virulence Factor Synthesis. *Nature Communications* **2017**, *8, 14631.*

50. Kralj, J. M.; Hochbaum, D. R.; Douglass, A. D.; Cohen, A. E. Electrical Spiking in *Escherichia coli* Probed with a Fluorescent Voltage-Indicating Protein. *Science* **2011**, *333* (6040), 345–348.

51. Zajdel, T. J.; TerAvest, M. A.; Rad, B.; Ajo-Franklin, C. M.; Maharbiz, M. M. Probing the Dynamics of the Proton-Motive Force in *E. coli*. In *IEEE SENSORS 2014 Proceedings*; IEEE: Valencia, Spain, 2014; pp 1764–1767.

52. Rojas, E. R.; Huang, K. C.; Theriot, J. A. Homeostatic Cell Growth Is Accomplished Mechanically through Membrane Tension Inhibition of Cell-Wall Synthesis. *Cell Systems* **2017**, *5* (6), 578-590.e6.

53. Rojas, E. R.; Huang, K. C. Regulation of Microbial Growth by Turgor Pressure. *Current Opinion in Microbiology* **2018**, *42*, 62–70.

54. Stratford, J. P.; Edwards, C. L. A.; Ghanshyam, M. J.; Malyshev, D.; Delise, M. A.; Hayashi, Y.; Asally, M. Electrically Induced Bacterial Membrane-Potential Dynamics Correspond to Cellular Proliferation Capacity. *Proceedings of the National Academy of Sciences* **2019**, *116* (19), 9552–9557.

55. Humphries, J.; Xiong, L.; Liu, J.; Prindle, A.; Yuan, F.; Arjes, H. A.; Tsimring, L.; Süel, G. M. Species-Independent Attraction to Biofilms through Electrical Signaling. *Cell* **2017**, *168* (1–2), 200-209.e12.

56. Bhattacharjee, A.; Datta, R.; Gratton, E.; Hochbaum, A. I. Metabolic Fingerprinting of Bacteria by Fluorescence Lifetime Imaging Microscopy. *Scientific Reports* **2017**, *7* (1), 3743.

57. Torno, K.; Wright, B. K.; Jones, M. R.; Digman, M. A.; Gratton, E.; Phillips, M. Real-Time Analysis of Metabolic Activity Within Lactobacillus Acidophilus by Phasor Fluorescence Lifetime Imaging Microscopy of NADH. *Current Microbiology* **2013**, *66* (4), 365–367.

58. Digman, M. A.; Caiolfa, V. R.; Zamai, M.; Gratton, E. The Phasor Approach to Fluorescence Lifetime Imaging Analysis. *Biophysical Journal* **2008**, *94* (2), L14–L16.

59. Lakowicz, J. R.; Szmacinski, H.; Nowaczyk, K.; Johnson, M. L. Fluorescence Lifetime Imaging of Free and Protein-Bound NADH. *Proceedings of the National Academy of Sciences* **1992**, *89*, 1271-1275.

60. Ali, M.; Lopez, A. L.; Ae You, Y.; Eun Kim, Y.; Sah, B.; Maskery, B.; Clemens, J. The Global Burden of Cholera. *Bulletin of the World Health Organization* **2012**, *90* (3), 209–218.

61. Bartlett, T. M.; Bratton, B. P.; Duvshani, A.; Miguel, A.; Sheng, Y.; Martin, N. R.; Nguyen, J. P.; Persat, A.; Desmarais, S. M.; VanNieuwenhze, M. S.; Huang, K. C.; Zhu, J.; Shaevitz, J. W.; Gitai, Z. A Periplasmic Polymer Curves *Vibrio cholerae* and Promotes Pathogenesis. *Cell* **2017**, *168* (1–2), 172-185.e15.

62. Utada, A. S.; Bennett, R. R.; Fong, J. C. N.; Gibiansky, M. L.; Yildiz, F. H.; Golestanian, R.; Wong, G. C. L. *Vibrio cholerae* Use Pili and Flagella Synergistically to Effect Motility Switching and Conditional Surface Attachment. *Nature Communications* **2014**, *5* (1), 4913.

63. Young, K. D. The Selective Value of Bacterial Shape. *Microbiology and Molecular Biology Reviews* **2006**, *70* (3), 660–703.

64. Teschler, J. K.; Zamorano-Sánchez, D.; Utada, A. S.; Warner, C. J. A.; Wong, G. C. L.; Linington, R. G.; Yildiz, F. H. Living in the Matrix: Assembly and Control of *Vibrio cholerae* Biofilms. *Nature Reviews Microbiology* **2015**, *13* (5), 255–268.

65. Imamura, H.; Huynh Nhat, K. P.; Togawa, H.; Saito, K.; Iino, R.; Kato-Yamada, Y.; Nagai, T.; Noji, H. Visualization of ATP Levels inside Single Living Cells with Fluorescence Resonance Energy Transfer-Based Genetically Encoded Indicators. *Proceedings of the National Academy of Sciences* **2009**, *106* (37), 15651–15656.

66. O'Loughlin, C. T.; Miller, L. C.; Siryaporn, A.; Drescher, K.; Semmelhack, M. F.; Bassler, B. L. A Quorum-Sensing Inhibitor Blocks *Pseudomonas aeruginosa* Virulence and Biofilm Formation. *Proceedings of the National Academy of Sciences* **2013**, *110* (44), 17981–17986.

67. Meng, Y.; Li, Y.; Galvani, C. D.; Hao, G.; Turner, J. N.; Burr, T. J.; Hoch, H. C. Upstream Migration of *Xylella Fastidiosa* via Pilus-Driven Twitching Motility. *Journal of Bacteriology* **2005**, *187*(16), 5560–5567.

68. Smith, E. E.; Buckley, D. G.; Wu, Z.; Saenphimmachak, C.; Hoffman, L. R.; D'Argenio, D. A.; Miller, S. I.; Ramsey, B. W.; Speert, D. P.; Moskowitz, S. M.; Burns, J. L.; Kaul, R.; Olson, M. V. Genetic Adaptation by *Pseudomonas aeruginosa* to the Airways of Cystic Fibrosis Patients. *Proceedings of the National Academy of Sciences* **2006**, *103* (22), 8487–8492.

69. Brown, L. M.; McComb, J. P.; Vangsness, M. D.; Bowen, L. L.; Mueller, S. S.; Balster, L. M.; Bleckmann, C. A. Community Dynamics and Phylogenetics of Bacteria Fouling Jet A and

JP-8 Aviation Fuel. *International Biodeterioration & Biodegradation* **2010**, *64* (3), 253–261.

70. Schultz, M. P.; Bendick, J. A.; Holm, E. R.; Hertel, W. M. Economic Impact of Biofouling on a Naval Surface Ship. *Biofouling* **2011**, *27* (1), 87–98.

71. Percival, S. L.; Walker, J. T. Potable Water and Biofilms: A Review of the Public Health Implications. *Biofouling* **1999**, *14* (2), 99–115.

72. Driscoll, J. A.; Brody, S. L.; Kollef, M. H. The Epidemiology, Pathogenesis and Treatment of *Pseudomonas aeruginosa* Infections: *Drugs* **2007**, *67* (3), 351–368.

73. Costerton, J. W. Bacterial Biofilms: A Common Cause of Persistent Infections. *Science* **1999**, *284* (5418), 1318–1322.

74. Mattick, J. S. Type IV Pili and Twitching Motility. *Annual Reviews Microbiology* **2002**, *56* (1), 289–314.

75. Howie, H. L.; Glogauer, M.; So, M. The N. Gonorrhoeae Type IV Pilus Stimulates Mechanosensitive Pathways and Cytoprotection through a PilT-Dependent Mechanism. *PLoS Biol* **2005**, *3* (4), e100.

76. Hill, J.; Kalkanci, O.; McMurry, J. L.; Koser, H. Hydrodynamic Surface Interactions Enable *Escherichia coli* to Seek Efficient Routes to Swim Upstream. *Physical Review Letters* **2007**, *98* (6), 068101.

77. Tsay, T.-B.; Jiang, Y.-Z.; Hsu, C.-M.; Chen, L.-W. *Pseudomonas aeruginosa* Colonization Enhances Ventilator-Associated Pneumonia-Induced Lung Injury. *Respir Res* **2016**, *17* (1), 101.

78. Lautrop, H. Bacterium Anitratum Transferred to the Genus Cytopgaga. *International Bulletin of Bacteriology Nomenclature Taxonomy* **1961**, 11, 107–108.

79. Henrichsen, J. Twitching Motility. *Annual Review Microbiology.* **1983**, *37* (1), 81–93.

80. Harshey, R. M. Bacterial Motility on a Surface: Many Ways to a Common Goal. *Annual Review Microbiology* **2003**, *57* (1), 249–273.

81. Jin, F.; Conrad, J. C.; Gibiansky, M. L.; Wong, G. C. L. Bacteria Use Type-IV Pili to Slingshot on Surfaces. *Proceedings of the National Academy of Sciences* **2011**, *108* (31), 12617–12622.

82. Giltner, C. L.; van Schaik, E. J.; Audette, G. F.; Kao, D.; Hodges, R. S.; Hassett, D. J.; Irvin, R. T. The *Pseudomonas aeruginosa* Type IV Pilin Receptor Binding Domain Functions as an Adhesin for Both Biotic and Abiotic Surfaces. *Molecular Microbiology* **2006**, *59* (4), 1083–1096.

83. Burrows, L. L. *Pseudomonas aeruginosa* Twitching Motility: Type IV Pili in Action. *Annual Review Microbiology* **2012**, *66* (1), 493–520.

84. Conrad, J. C.; Gibiansky, M. L.; Jin, F.; Gordon, V. D.; Motto, D. A.; Mathewson, M. A.; Stopka, W. G.; Zelasko, D. C.; Shrout, J. D.; Wong, G. C. L. Flagella and Pili-Mediated Near-Surface Single-Cell Motility Mechanisms in *P. aeruginosa*. *Biophysical Journal* **2011**, *100* (7), 1608–1616.

85. Brill-Karniely, Y.; Jin, F.; Wong, G. C. L.; Frenkel, D.; Dobnikar, J. Emergence of Complex Behavior in Pili-Based Motility in Early Stages of *P. aeruginosa* Surface Adaptation. *Scientific Reports* **2017**, *7*(1), 45467.

86. Maier, B.; Wong, G. C. L. How Bacteria Use Type IV Pili Machinery on Surfaces. *Trends in Microbiology* **2015**, *23* (12), 775–788.

87. Cowles, K. N.; Gitai, Z. Surface Association and the MreB Cytoskeleton Regulate Pilus Production, Localization and Function in *Pseudomonas aeruginosa*: *Pseudomonas* Pilus Regulation and MreB. *Molecular Microbiology* **2010**, *76* (6), 1411–1426.

88. Shen, Y.; Siryaporn, A.; Lecuyer, S.; Gitai, Z.; Stone, H. A. Flow Directs Surface-Attached Bacteria to Twitch Upstream. *Biophysical Journal* **2012**, *103* (1), 146–151.

89. Bertrand, J. J.; West, J. T.; Engel, J. N. Genetic Analysis of the Regulation of Type IV Pilus Function by the Chp Chemosensory System of *Pseudomonas aeruginosa. Journal of Bacteriology***2010**, *192* (4), 994–1010.

90. Merz, A. J.; So, M.; Sheetz, M. P. Pilus Retraction Powers Bacterial Twitching Motility. *Nature* **2000**, *407* (6800), 98–102.

91. Skerker, J. M.; Berg, H. C. Direct Observation of Extension and Retraction of Type IV Pili. *Proceedings of the National Academy of Sciences* **2001**, *98* (12), 6901–6904.

92. Tala, L.; Fineberg, A.; Kukura, P.; Persat, A. *Pseudomonas aeruginosa* Orchestrates Twitching Motility by Sequential Control of The Type IV Pili Movements. *Nature Microbiology* **2019**, *4*, 774-780.

93. Maier, B.; Potter, L.; So, M.; Seifert, H. S.; Sheetz, M. P. Single Pilus Motor Forces Exceed 100 PN. *Proceedings of the National Academy of Sciences* **2002**, *99* (25), 16012–16017.

94. Beaussart, A.; Baker, A. E.; Kuchma, S. L.; El-Kirat-Chatel, S.; O'Toole, G. A.; Dufrêne, Y. F. Nanoscale Adhesion Forces of *Pseudomonas aeruginosa* Type IV Pili. *ACS Nano* **2014**, *8* (10), 10723–10733.

95. Siryaporn, A.; Kim, M. K.; Shen, Y.; Stone, H. A.; Gitai, Z. Colonization, Competition, and Dispersal of Pathogens in Fluid Flow Networks. *Current Biology* **2015**, *25* (9), 1201–1207.

96. Anyan, M. E.; Amiri, A.; Harvey, C. W.; Tierra, G.; Morales-Soto, N.; Driscoll, C. M.; Alber, M. S.; Shrout, J. D. Type IV Pili Interactions Promote Intercellular Association and Moderate Swarming of *Pseudomonas aeruginosa*. *Proceedings of the National Academy of Sciences* **2014**, *111* (50), 18013–18018.

97. Persat, A.; Inclan, Y. F.; Engel, J. N.; Stone, H. A.; Gitai, Z. Type IV Pili Mechanochemically Regulate Virulence Factors in *Pseudomonas aeruginosa*. *Proceedings of the National Academy of Sciences* **2015**, *112* (24), 7563–7568.

98. Inclan, Y. F.; Persat, A.; Greninger, A.; Von Dollen, J.; Johnson, J.; Krogan, N.; Gitai, Z.; Engel, J. N. A Scaffold Protein Connects Type IV Pili with the Chp Chemosensory System to Mediate Activation of Virulence Signaling in *Pseudomonas aeruginosa*: FimL Connects Type IV Pili with the Chp Chemosensory System. *Molecular Microbiology* **2016**, *101* (4), 590–605.

99. Conrad, J. C. Physics of Bacterial Near-Surface Motility Using Flagella and Type IV Pili: Implications for Biofilm Formation. *Research in Microbiology* **2012**, *163* (9–10), 619–629.

100. Rodesney, C. A.; Roman, B.; Dhamani, N.; Cooley, B. J.; Katira, P.; Touhami, A.; Gordon, V. D. Mechanosensing of Shear by *Pseudomonas aeruginosa* Leads to Increased Levels of the Cyclic-Di-GMP Signal Initiating Biofilm Development. *Proceedings of the National Academy of Sciences* **2017**, *114* (23), 5906–5911.

101. Chang, Y.-R.; Weeks, E. R.; Ducker, W. A. Surface Topography Hinders Bacterial Surface Motility. *ACS Applies Materials and Interfaces* **2018**, *10* (11), 9225–9234.

102. Jaggessar, A.; Shahali, H.; Mathew, A.; Yarlagadda, P. K. D. V. Bio-Mimicking Nano and Micro-Structured Surface Fabrication for Antibacterial Properties in Medical Implants. *J Nanobiotechnol* **2017**, *15* (1), 64.

103. Anselme, K.; Davidson, P.; Popa, A. M.; Giazzon, M.; Liley, M.; Ploux, L. The Interaction of Cells and Bacteria with Surfaces Structured at the Nanometre Scale. *Acta Biomaterialia* **2010**, *6*(10), 3824–3846.

104. Bocquet, L.; Barrat, J.-L. Flow Boundary Conditions from Nano- to Micro-Scales. *Soft Matter* **2007**, *3* (6), 685.

105. Bhushan, B. Biomimetics Inspired Surfaces for Drag Reduction and Oleophobicity/ Philicity. *Beilstein J. Nanotechnol.* **2011**, *2*, 66–84.

106. Cottin-Bizonne, C.; Barrat, J.-L.; Bocquet, L.; Charlaix, E. Low-Friction Flows of Liquid at Nanopatterned Interfaces. *Nature Materials* **2003**, *2* (4), 237–240.

107. Govardhan, R. N.; Srinivas, G. S.; Asthana, A.; Bobji, M. S. Time Dependence of Effective Slip on Textured Hydrophobic Surfaces. *Physics of Fluids* **2009**, *21* (5), 052001.

108. Krams, R.; Wentzel, J. J.; Cespedes, I.; Vinke, R.; Carlier, S.; van der Steen, A. F. W.; Lancee, C. T.; Slager, C. J. Effect of Catheter Placement on 3-D Velocity Profiles in Curved Tubes Resembling the Human Coronary System. *Ultrasound in Medicine & Biology* **1999**, *25* (5), 803–810.

109. Tinevez, J.-Y.; Perry, N.; Schindelin, J.; Hoopes, G. M.; Reynolds, G. D.; Laplantine, E.; Bednarek, S. Y.; Shorte, S. L.; Eliceiri, K. W. TrackMate: An Open and Extensible Platform for Single-Particle Tracking. *Methods* **2017**, *115*, 80–90.

110. Lecuyer, S.; Rusconi, R.; Shen, Y.; Forsyth, A.; Vlamakis, H.; Kolter, R.; Stone, H. A. Shear Stress Increases the Residence Time of Adhesion of *Pseudomonas aeruginosa*. *Biophysical Journal* **2011**, *100* (2), 341–350.

111. Zhang, G.; Zhang, J.; Xie, G.; Liu, Z.; Shao, H. Cicada Wings: A Stamp from Nature for Nanoimprint Lithography. *Small* **2006**, *2* (12), 1440–1443.

112. Odom, T. W.; Love, J. C.; Wolfe, D. B.; Paul, K. E.; Whitesides, G. M. Improved Pattern Transfer in Soft Lithography Using Composite Stamps. *Langmuir* **2002**, *18* (13), 5314–5320.

113. Kang, H.; Lee, J.; Park, J.; Lee, H. H. An Improved Method of Preparing Composite Poly(Dimethylsiloxane) Moulds. *Nanotechnology* **2006**, *17* (1), 197–200.

114. Perfect, J. R. The Antifungal Pipeline: A Reality Check. *Nature Reviews Drug Discovery* **2017**, *16* (9), 603–616.

115. Havlickova, B.; Czaika, V. A.; Friedrich, M. Epidemiological Trends in Skin Mycoses Worldwide. *Mycoses* **2008**, *51*, 2–15.

116. Brown, G. D.; Denning, D. W.; Gow, N. A. R.; Levitz, S. M.; Netea, M. G.; White, T. C. Hidden Killers: Human Fungal Infections. *Science Translational Medicine* **2012**, *4* (165), 165rv13-165rv13.

117. Lupetti, A. Molecular Basis of Resistance to Azole Antifungals. *Trends in Molecular Medicine* **2002**, *8* (2), 76–81.

118. Vivek-Ananth, R. P.; Mohanraj, K.; Vandanashree, M.; Jhingran, A.; Craig, J. P.; Samal, A. Comparative Systems Analysis of the Secretome of the Opportunistic Pathogen

Aspergillus fumigatus and Other *Aspergillus* Species. *Scientific Reports* **2018**, *8* (1), 6617.

119. Kim, H.-S.; Kim, J.-E.; Frailey, D.; Nohe, A.; Duncan, R.; Czymmek, K. J.; Kang, S. Roles of Three *Fusarium oxysporum* Calcium Ion (Ca2+) Channels in Generating Ca2+ Signatures and Controlling Growth. *Fungal Genetics and Biology* **2015**, *82*, 145–157.

120. De Groot, P. W. J.; Ram, A. F.; Klis, F. M. Features and Functions of Covalently Linked Proteins in Fungal Cell Walls. *Fungal Genetics and Biology* **2005**, *42* (8), 657–675.

121. Zhou, L.; Evangelinos, M.; Wernet, V.; Eckert, A. F.; Ishitsuka, Y.; Fischer, R.; Nienhaus, G. U.; Takeshita, N. Superresolution and Pulse-Chase Imaging Reveal the Role of Vesicle Transport in Polar Growth of Fungal Cells. *Science Advances* **2018**, *4* (1), e1701798.

122. Enjalbert, B.; Whiteway, M. Release from Quorum-Sensing Molecules Triggers Hyphal Formation during *Candida albicans* Resumption of Growth. *Eukaryotic Cell* **2005**, *4* (7), 1203–1210.

123. Ramage, G.; Mowat, E.; Jones, B.; Williams, C.; Lopez-Ribot, J. Our Current Understanding of Fungal Biofilms. *Critical Reviews in Microbiology* **2009**, *35* (4), 340–355.

124. Rauch, M. E.; Graef, H. W.; Rozenzhak, S. M.; Jones, S. E.; Bleckmann, C. A.; Kruger, R. L.; Naik, R. R.; Stone, M. O. Characterization of Microbial Contamination in United States Air Force Aviation Fuel Tanks. *J IND MICROBIOL BIOTECHNOL* **2006**, *33* (1), 29–36.

125. Silveira, F. P.; Husain, S. Fungal Infections in Solid Organ Transplantation. *Med Mycol* **2007**, *45* (4), 305–320.

126. Anderson, J. B. Evolution of Antifungal-Drug Resistance: Mechanisms and Pathogen Fitness. *Nature Review Microbiology* **2005**, *3* (7), 547–556.

127. Kang, X.; Kirui, A.; Muszyński, A.; Widanage, M. C. D.; Chen, A.; Azadi, P.; Wang, P.; Mentink-Vigier, F.; Wang, T. Molecular Architecture of Fungal Cell Walls Revealed by Solid-State NMR. *Nature Communications* **2018**, *9* (1), 2747.

128. Bartnicki-Garcia, S.; Bracker, C. E.; Gierz, G.; López-Franco, R.; Lu, H. Mapping the Growth of Fungal Hyphae: Orthogonal Cell Wall Expansion during Tip Growth and the Role of Turgor. *Biophysical Journal* **2000**, *79* (5), 2382–2390.

129. Baldauf, S. L. A Kingdom-Level Phylogeny of Eukaryotes Based on Combined Protein Data. *Science* **2000**, *290* (5493), 972–977.

130. Paulo, C. S. O.; Vidal, M.; Ferreira, L. S. Antifungal Nanoparticles and Surfaces. *Biomacromolecules* **2010**, *11* (10), 2810–2817.

131. Shrestha, S. K.; Fosso, M. Y.; Garneau-Tsodikova, S. A Combination Approach to Treating Fungal Infections. *Scientific Reports* **2015**, *5* (1), 17070.

132. Nowlin, K.; Boseman, A.; Covell, A.; LaJeunesse, D. Adhesion-Dependent Rupturing of *Saccharomyces cerevisiae* on Biological Antimicrobial Nanostructured Surfaces. *J. R. Soc. Interface***2015**, *12* (102), 20140999.

133. Chang, Y.-W.; Rettberg, L. A.; Treuner-Lange, A.; Iwasa, J.; Søgaard-Andersen, L.; Jensen, G. J. Architecture of the Type IVa Pilus Machine. *Science* **2016**, *351* (6278), aad2001.

134. Amir, A.; Babaeipour, F.; McIntosh, D. B.; Nelson, D. R.; Jun, S. Bending Forces Plastically Deform Growing Bacterial Cell Walls. *Proceedings of the National Academy of Sciences* **2014**, *111* (16), 5778–5783.

135. Furchtgott, L.; Wingreen, N. S.; Huang, K. C. Mechanisms for Maintaining Cell Shape in Rod-Shaped Gram-Negative Bacteria: Rod-Shape Maintenance in Gram-Negative Bacteria. *Molecular Microbiology* **2011**, *81* (2), 340–353.

136. Lo, H-J,; Kohler, J. R.; DiDomenico, B.; Loebenberg, D.; Cacciapuoti, A.; Fink, G. R. Nonfilamentous *C. albicans* Mutants Are Avirulent. *Cell* **1997**, *99*, 939-949.

137. Madhani, H. D.; Fink, G. R. The Control of Filamentous Differentiation and Virulence in Fungi. *Cell Biology* **1998**, *8*, 348-353.

138. Cetiner, U.; Rowe, I.; Schams, A.; Mayhew, C.; Rubin, D.; Anishkin, A.; Sukharev, S. Tension-Activated Channels in the Mechanism of Osmotic Fitness in *Pseudomonas aeruginosa*. *The Journal of General Physiology* **2017**, *149* (5), 595–609.

139. Compton, E. L. R.; Mindell, J. A. Bacterial Ion Channels. *EcoSal Plus* **2010**, *4* (1).

140. Chure, G.; Lee, H. J.; Rasmussen, A.; Phillips, R. Connecting the Dots between Mechanosensitive Channel Abundance, Osmotic Shock, and Survival at Single-Cell Resolution. *J Bacteriol* **2018**, *200* (23), e00460-18, /jb/200/23/e00460-18.atom.

141. Cox, C. D.; Bavi, N.; Martinac, B. Bacterial Mechanosensors. *Annuual Review of Physiology* **2018**, *80* (1), 71–93.

142. Haswell, E. S.; Phillips, R.; Rees, D. C. Mechanosensitive Channels: What Can They Do and How Do They Do It? *Structure* **2011**, *19* (10), 1356–1369.

143. Bezanilla, F.; Perozo, E. Force and Voltage Sensors in One Structure. *Science* **2002**, *298*, 1562-1563.

144. Bruni, G. N.; Weekley, R. A.; Dodd, B. J. T.; Kralj, J. M. Voltage-Gated Calcium Flux

Mediates *Escherichia coli* Mechanosensation. *Proceedings of the National Academy of Sciences* **2017**, *114* (35), 9445–9450.

145. Bialecka-Fornal, M.; Lee, H. J.; DeBerg, H. A.; Gandhi, C. S.; Phillips, R. Single-Cell Census of Mechanosensitive Channels in Living Bacteria. *PLoS ONE* **2012**, *7* (3), e33077.

146. Bialecka-Fornal, M.; Lee, H. J.; Phillips, R. The Rate of Osmotic Downshock Determines the Survival Probability of Bacterial Mechanosensitive Channel Mutants. *Journal of Bacteriology* **2015**, *197* (1), 231–237.

147. Rojas, E.; Theriot, J. A.; Huang, K. C. Response of *Escherichia coli* Growth Rate to Osmotic Shock. *Proceedings of the National Academy of Sciences* **2014**, *111* (21), 7807–7812.

148. Prindle, A.; Liu, J.; Asally, M.; Ly, S.; Garcia-Ojalvo, J.; Süel, G. M. Ion Channels Enable Electrical Communication in Bacterial Communities. *Nature* **2015**, *527* (7576), 59–63.

149. Scott, M.; Gunderson, C. W.; Mateescu, E. M.; Zhang, Z.; Hwa, T. Interdependence of Cell Growth and Gene Expression: Origins and Consequences. *Science* **2010**, *330* (6007), 1099–1102.

150. Lee, C. K.; de Anda, J.; Baker, A. E.; Bennett, R. R.; Luo, Y.; Lee, E. Y.; Keefe, J. A.; Helali, J. S.; Ma, J.; Zhao, K.; Golestanian, R.; O'Toole, G. A.; Wong, G. C. L. Multigenerational Memory and Adaptive Adhesion in Early Bacterial Biofilm Communities. *Proceedings of the National Academy of Sciences* **2018**, *115* (17), 4471–4476.